Tectonophysics 913 (2025) 230881

Contents lists available at ScienceDirect

Tectonophysics

journal homepage: www.elsevier.com/locate/tecto

Density perturbations in the crust indicate potential for blind magmatism beneath magma-poor rifts

Emmanuel A. Njinju [a,b,*], Folarin Kolawole [c], Estella A. Atekwana [b], Rasheed Ajala [c], Eliot A. Atekwana [b], D. Sarah Stamps [d], Rob.L. Evans [e], Andrew Katumwehe [f], Peter H. Barry [g], Suzan van der Lee [h], John Mary Kiberu [i], Fred Tugume [j], Albert Kabanda [h], Michael Taylor [k], Joan Nakajigo [i], Abbey Oluwasegun Isaac [f]

[a] Now at the Department of Geosciences, Baylor University, Waco, TX, USA
[b] Department of Earth & Planetary Sciences, University of California Davis, Davis, CA, USA
[c] Department of Earth & Environmental Sciences, Columbia University, New York, NY, USA
[d] Department of Geosciences, Virginia Tech, Blacksburg, VA, USA
[e] Department of Geology and Geophysics, Woods Hole Oceanographic Institution, Woods Hole, MA, USA
[f] Kimbell School of Geosciences, Midwestern State University, Wichita Falls, TX, USA
[g] Department of Marine Chemistry and Geochemistry, Woods Hole Oceanographic Institution, Woods Hole, MA, USA
[h] Department of Earth, Environmental, and Planetary Sciences, Northwestern University, Evanston, IL, USA
[i] Department of Geology and Petroleum Studies, Makerere University, Kampala, Uganda
[j] Ministry of Energy and Mineral Development (MEMD), Uganda
[k] Department of Geology, University of Kansas, Lawrence, KS, USA

ARTICLE INFO

Keywords:
Non-volcanic rifting
Magma-poor rifting, Field mapping
Gravity inversion
Density perturbations
Forward gravity modeling
Seismic constraints
Blind magmatism
Crustal structure

ABSTRACT

Lithospheric weakening mechanisms in non-volcanic segments of active continental rifts remain poorly understood, raising important questions about the geodynamic processes that drive magma-poor rifting. Here, we investigate the crustal and uppermost mantle structure beneath the non-volcanic Albertine-Rhino Graben (ARG) and the adjoining volcanic Edward-George Rift (EGR), East Africa. The ARG exhibits anomalous focusing of intra-rift faulting typically associated with magma-rich, early-stage rifts. Through field observations of rift structures, combined with 3D inversions and 2D forward modeling of gravity data, we investigate the potential controls on intra-rift tectonic strain in a setting with little to no magmatism. Field ground-truthing in the southern ARG reveals prominent rift-axial basement-rooted faulting that post-dates the establishment of border faults. Gravity inversion results show low-density anomalies extending from the surface to about 50 km depth beneath both the EGR and southern ARG, with the strongest anomalies under the ARG at around 15 km. 2D gravity modeling suggests that the lower crust and uppermost mantle are both thinned and less dense beneath these rift segments. In the EGR, crustal thinning and low-density anomalies align with low P-wave velocity zones, suggesting the presence of melt. Given the similar degree of crustal thinning and de-densification in the southern ARG, we infer that trapped lower-crustal melts may also exist beneath the rift, potentially contributing to the early focusing of intra-rift strain. We propose that in non-volcanic rifts, deep, unexposed ('blind') melts may play a key role in mechanical weakening of the lithosphere, enabling continued tectonic extension even in the absence of significant surface volcanism.

1. Introduction

Continental rifting plays a key role in global tectonics as it initiates plate divergence and determines the locations of the creation of new lithosphere (Wilson, 1966). Yet, fundamental questions related to mechanisms that drive rift initiation remain largely unanswered. The "tectonic force paradox" indicates that the available tectonic forces required to initiate and sustain the rifting of cold, thick, continental lithosphere are insufficient to overcome the strength of the lithosphere (e.g., Buck, 2006; Stamps et al., 2010, 2014; Brune et al., 2023).

* Corresponding author at: Now at the Department of Geosciences, Baylor University, Waco, TX, USA.
E-mail address: emmanuel_njinju@baylor.edu (E.A. Njinju).

https://doi.org/10.1016/j.tecto.2025.230881
Received 19 February 2025; Received in revised form 12 August 2025; Accepted 16 August 2025
Available online 18 August 2025

However, continental break-up can be initiated if the lithosphere has been thermally and mechanically weakened through magmatic processes (e.g., Buck, 2006; Koptev et al., 2015; Schmeling, 2010) either from an upwelling asthenosphere or from mantle plumes (Njinju et al., 2021; Njinju et al., 2023a; Rajaonarison et al., 2023). This magma-assisted rifting model is supported by extensive volcanism within many rift systems, such as the Eastern Branch of the East African Rift System (EARS) (Fig. 1A) (Ebinger, 2005; Kendall et al., 2005). Nevertheless, there are many areas on Earth where active rifting occurs without presence of volcanism. For example, the Western Branch of the EARS (Fig. 1A) only exhibits volcanism within a few areas, including the Toro-Ankole (~0.6 Ma), Virunga (~12.6 Ma), South Kivu (~21 Ma), Mwenga-Kamituga (5.8 – 2.6 Ma), and the Rungwe (~8.6 Ma) Volcanic Provinces (Ebinger, 1989; Kampunzu et al., 1998; Halldórsson et al., 2014; Colet et al., 2025), marking a contrast between this branch and the Eastern Branch of the EARS. The existence of non-volcanic active rift segments raises key questions about the role that melts play in initiating and driving progressive continental rifting. In other words, is rifting assisted by low-volume melts deep beneath actively extending non-volcanic rifts, which are yet to breach the surface, as proposed in the 'blind melt' rifting model of Ajala et al. (2024)? Or do non-volcanic rifts lack deep melts, indicating the control of other strain-localization mechanisms in the lithosphere? Blind magmatism, with even relatively small amounts of melts, can heat the lithosphere and weaken it by an order of magnitude, allowing for rifting to continue even without continuous melt input (Bialas et al., 2010).

We address these questions by examining the northern Western Branch of the EARS, which hosts contiguous volcanic and non-volcanic rift segments, thus presenting a tectonic setting that offers a unique opportunity to study the along-axis transition from magma-rich to

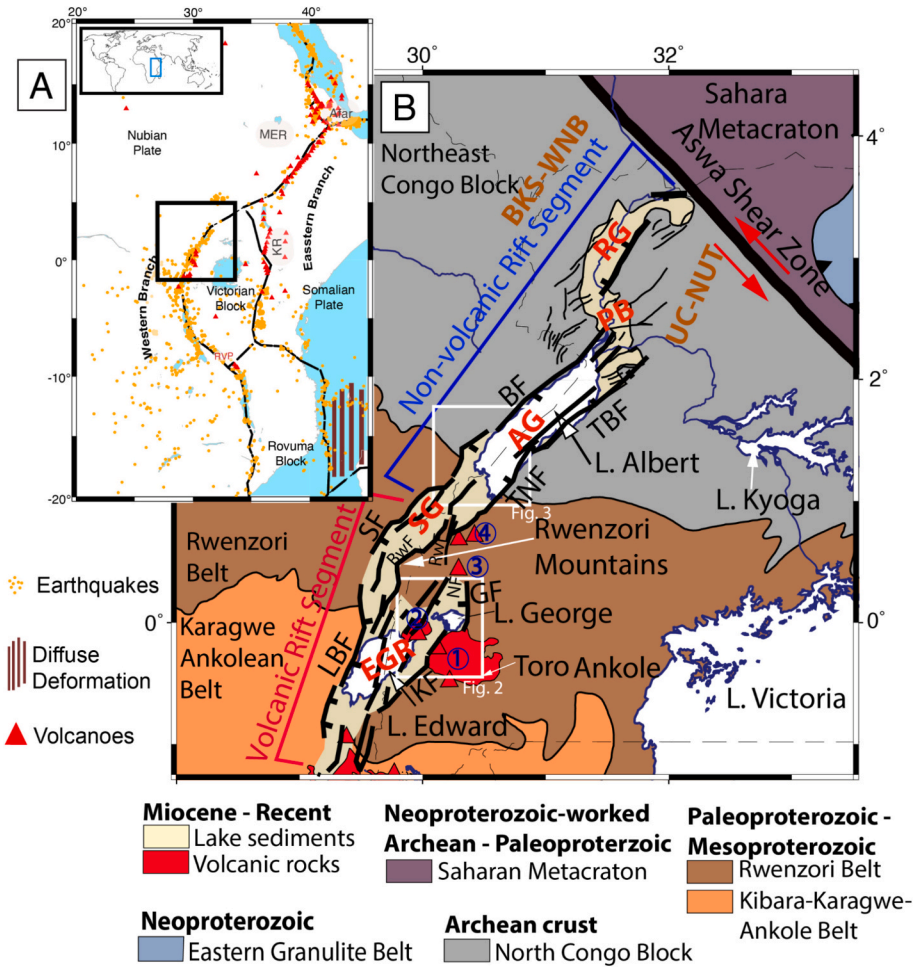

Fig. 1. (**A**) Map of the East African Rift System (EARS) with the Eastern and Western Branches outlined by plate boundaries from Stamps et al. (2008, 2018). The earthquakes (orange dots) with >M2 (2000–2020) are obtained from the NEIC catalog (Beauval et al., 2013), and the Holocene volcanoes (red triangles) are from the Global Volcanism Program (2023). The inset map shows the relative location of part of the EARS (blue rectangle) in Africa. The diffuse deformation offshore of the Eastern Branch is based on a geodetic study by Stamps et al. (2021). MER = Main Ethiopian Rift. KR = Kenyan Rift. The black box shows the location of the northern Western Branch (Fig. 1B). (**B**) Tectonic map of the northern Western Branch of the EARS, modified after Fritz et al. (2013) and Katumwehe et al. (2015). Red triangles and red outlines represent Miocene-Recent volcanic rocks of the Toro-Ankole Volcanic Province (TAVP) with spatial extent modified from Nyakecho and Hagemann (2014). The numbers in blue circles represent the four main volcanic centers of the TAVP, which are (1) Bunyaruguru, (2) Katwe-Kikorongo, (3) Kyatwa, and (4) Kichwamba volcanoes. The volcanic Edward-George Rift (EGR) connects northward to the non-magmatic Albertine-Rhino Graben (ARG) through the Semliki Graben (SG) located at the western flank of the Rwenzori Mountains. The northern non-volcanic segment extends through Lake Albert (Albertine Graben, AG) and the Rhino Graben (RG) and terminates against the Aswa Shear Zone. PB = Pakwach Basin. The black lines are faults from the Global Earthquake Model Foundation's (GEM) Global Active Faults Database (GAF-DB; Styron and Pagani, 2020). BF = Bunia Fault. TNF = Tonya Fault. TBF = Toro-Bunyoro Fault. BKS-WNB = Bomu-Kibalian Shield - West Nile Block. UC-NUT = Ugandan Craton - Northern Uganda Terrane. LBF = Lubero Border Fault. SF = Semliki Fault. GF = George Fault. KibF = Kibuku Fault. KF = Kichwamba Fault. BwF = Bwamba Fault. RWF = Ruimi-Wasa Fault. NF = Nyamwamba Fault. White boxes labeled Fig. 2 and Fig. 3 show the locations of field observations, i.e., Figs. 2 and 3, respectively. (For interpretation of the references to colour in this figure legend, the reader is referred to the web version of this article.)

magma-poor rifting. This non-volcanic rift segment hosts intra-rift faulting with anomalous surface uplift. Such focused intra-rift deformation is commonly observed in magma-rich early-stage rifts (Muirhead et al., 2019;Wedmore et al., 2024), which poses questions about the subsurface crustal structure that is responsible for such anomalous strain accommodation. We hypothesize that crustal thinning facilitates the infiltration of mantle-derived fluids into the lower crust, enabling further thinning by increasing crustal buoyancy and focused intra-rift faulting within the non-volcanic rift segment. To characterize the possible controls on tectonic strain without voluminous magmatism and to test if crustal buoyancy contributes to the development of the mapped structures, we conducted field mapping of rift structures and performed 3D inversions and 2D forward modeling of gravity data to model the associated subsurface density structure.

Field mapping highlights anomalous post-Pleistocene uplift on a prominent basement-rooted intra-rift fault in the non-volcanic rift segment, collocated with intracrustal negative density anomalies. These anomalous lower density anomalies are reminiscent of low P-wave velocity anomalies beneath the volcanic rift segment just south of the location (Jakovlev et al., 2013), where our gravity inversion also resolves negative density anomalies. In this volcanic segment, previous studies have imaged thinned crust using seismic receiver function estimates (Gummert et al., 2016; Wölbern et al., 2010, 2012) and seismic anisotropy in the crust from shear wave splitting analysis, both suggesting the infiltration of melt beneath the rift zone and the Rwenzori Mountains (Batte et al., 2014). In this study, we assume the Rwenzori Mountains are associated with the volcanic rift segment (Fig. 1B). There is more evidence of magmatism in the volcanic rift segment from the distribution of seismicity, suggesting the presence of vertical magmatic fluid migration within faults along the Rwenzori Mountains (Lindenfeld et al., 2012). There is further support for partial melt beneath the volcanic rift segment from the imaging of conductive anomalies from magnetotelluric data at a depth of ~15–20 km beneath the Toro-Ankole Volcanic Province (Häuserer and Junge, 2011). Our two-dimensional forward gravity modeling supports evidence of de-densification of the lower-crust beneath both the volcanic and non-volcanic rift segments. We interpret this de-densification as a result of deep crustal and/or uppermost mantle melting. This inferred unerupted melt lowers the strength of the lithosphere, which facilitates rifting of this and other non-volcanic rift segments.

2. Geological and tectonic setting

The Cenozoic EARS consist of the magma-rich Eastern Branch and the magma-poor Western Branch (Fig. 1A; Njinju et al., 2019a,b). Geodetic studies using Global Position System (GPS) measurements, earthquakes slip vectors, and transform fault azimuth data, suggest that the Western Branch is governed by an eastward movement and counterclockwise rotation of the Victoria Block away from the Nubian Plate with relative velocities increasing from ~1.1 mm/year in the north to ~2.9 mm/year in the south (Fig. 1A; Calais et al., 2006; Stamps et al., 2008; Saria et al., 2014).

Radiometric dating of volcanic tuffs using $^{40}Ar/^{39}Ar$, detrital zircons, and U—Pb systematics suggests that by 26–25 Ma, the Western Branch was well-developed with rift segments bounded by border faults and uplifted rift flanks (Roberts et al., 2012). Numerical geodynamic modeling suggests that both the magma-rich Eastern Branch and the magma-poor Western Branch develop concomitantly due to the impingement of a mantle plume beneath the Tanzanian Craton preferentially to the east, leading to more magmatism in the Eastern Branch (Koptev et al., 2015). The Koptev et al. (2015) model advocates for thinning of the lithosphere to create channels that serve as conduits for transporting mantle plume material, and this is supported by a record of elevated mantle potential temperatures in Neogene volcanic rocks in the region (i.e., Rooney et al., 2012).

The northern Western Branch of the EARS hosts contiguous volcanic and non-volcanic rift segments (Fig. 1B). The volcanic segment consists of the Lakes Edward-George Rift (EGR) in the SW, within the Toro Ankole Volcanic Province, while the non-volcanic segment comprises the Albertine-Rhino Graben (ARG) in the NE (Fig. 1B). The EGR is extending within the Paleoproterozoic-Mesoproterozoic Rwenzori and the Kibara-Karagwe-Ankole orogenic belts (Fig. 1B; Begg et al., 2009; Tack et al., 2010; Link et al., 2010; Westerhof et al., 2014). The EGR consists of two half-grabens, i.e., the Lake Edward Rift to the west and the Lake George Rift to the east, separated by a NW-SE trending accommodation zone (Lærdal, 2002). The Lake Edward Rift is bordered to the west by the well-developed Lubero Border Fault (LBF) and to the east by the less-developed Kichwamba Fault (KF) (Fig. 1B). The Lake George Rift is bordered to the west by the Nyamwamba Fault (NF) and to the east by the George Fault (GF) (Fig. 1B). In general, the EGR is undergoing magma-assisted rifting, primarily due to the presence of magma underneath the Toro-Ankole Volcanic Province, which comprises four main volcanic centers. The Bunyaruguru and Katwe-Kikorongo volcanoes are located within the basement high accommodation zone (Fig. 1B) along the border faults of the Lake George Rift (i.e., the GF and Nyamwamba Fault, respectively). The Kyatwa and Kichwamba volcanoes are situated north of the GF (Fig. 1B). The Bunyaruguru and Katwe-Kikorongo volcanic fields of the Toro-Ankole Volcanic Province (Figs. 1B and 2A) consist of Pleistocene explosive volcanic craters producing maar volcanoes and tuff rings (Lærdal, 2002; Corti et al., 2013). Some of the volcanic craters are characterized by the presence of hot springs (Bahati et al., 2005) with isotopic compositions suggestive of a mantle lithospheric origin (Rosenthal et al., 2009; Foley et al., 2012). The magma-rich EGR is connected to the non-volcanic ARG via the Semliki Graben (SG) on the western flank of the Rwenzori Mountain, which is a ~ 5 km high uplifted horst block of Precambrian basement (Fig. 1B).

The northern non-volcanic rift segment, i.e., the ARG, extends through Lake Albert (as the Albertine Graben, AG) and further north as the Rhino Graben (RG) through the Pakwach Basin (PB) (Fig. 1B). The southernmost portion of AG hosts anomalous focusing of intra-rift tectonic strain along the Kibuku Fault (Fig. 1B), commonly observed only in magma-rich early-stage rifts. The asymmetric full AG is ~60 to 80 km-wide and is bounded to the west by the Bunia Fault with escarpment reaching ~1700 m in places and bounded to the east by the Tonya Fault and the Toro-Bunyoro Fault (Fig. 1B). The AG is filled with early Miocene-late Pleistocene sedimentary rocks, mainly lacustrine sandstone, organic-rich shales, siltstone, and conglomerates (Karp et al., 2012). The main depocenter of the AG is along the Bunia Fault in the NW with sedimentary thickness reaching ~5400 m compared to ~1250 m in the SE depocenter along the Tonya Fault (Upcott et al., 1996; Ring, 2008; Karp et al., 2012). The RG is an asymmetric half-graben that switches polarity from the SW to the NE. The southwestern portion of the RG is a ~ 40 km wide SE-dipping half-graben, and the northeastern portion of the RG consists of a ~ 10 km wide NW-dipping half-graben. (Fig. 1B; Katumwehe et al., 2015).

Most of the ARG is extending within the Archean-Paleoproterozoic NE Congo Block except for its southwestern-most portion, where the Paleoproterozoic-Mesoproterozoic Rwenzori orogenic belt is exposed (Fig. 1B; Tack et al., 2010; Fernandez-Alonso et al., 2012; Nyakecho and Hagemann, 2014). The NE Congo Block is an exposure of the Congo Craton in northeastern Congo and northwestern Uganda and is subdivided into the Bomu-Kibalian Shield-West Nile Block (BKS-WNB; Fig. 1B) in the west and the Ugandan Craton-North Uganda Terrane (UC-NUT; Fig. 1B) to the east (Begg et al., 2009; Westerhof et al., 2014). The boundary between the BKS-WNB and the UC-NUT is characterized by exposures of ultra-high-pressure granulite metamorphic rocks that formed ~2.4 Ga (Begg et al., 2009). The ARG traces the boundary of these cratonic blocks (Fig. 1B; Begg et al., 2009; Link et al., 2010; Westerhof et al., 2014). This intracratonic boundary consists of the narrow Mesoproterozoic-Neoproterozoic Madi-Igisi Belt in NW Uganda, characterized by several SE and NW-verging Precambrian thrust faults

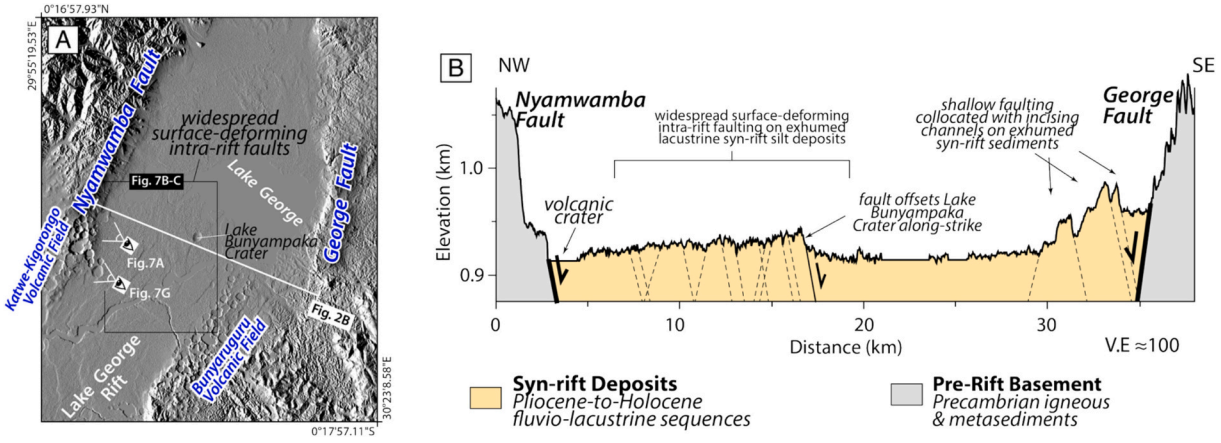

Fig. 2. (**A**) Topographic relief map (Shuttle Radar Topographic Mission, SRTM) of the magma-rich Lake George Rift. We note the volcanic fields in both the border fault zone and within the rift axis, as well as the region of widespread surface-deforming intra-rift faulting at the rift floor. **(B)** Topographic relief profile across the Lake George Rift highlighting a prominent surface-breaking intra-rift fault and the region of widespread intra-rift surface faulting in its footwall. See details in Fig. 7. V.E = vertical exaggeration. Note that the illustrated fault dips in Fig. 2B are hypothetical and not measured.

(Westerhof et al., 2014). The ARG terminates at the NW-trending Neoproterozoic Aswa Shear Zone (Katumwehe et al., 2015), which is a lithospheric-scale boundary between the Northeast Congo Block to the southwest and the Saharan Metacraton to the northeast (Fig. 1B; Abdelsalam et al., 2002, 2011; Katumwehe et al., 2015).

3. Data and methods

3.1. Field mapping of intra-rift faulting

As part of the NSF-funded project entitled "Dry-Rifting In the Albertine-Rhino graben (DRIAR), Uganda", we perform field examinations of the surface scarps observable on topographic maps of the rift axes of the magma-rich Lake George Rift (Figs. 2A-B) and magma-poor southern Albertine Rift (Figs. 3A-B and profiles in Figs. 3C-E). We aim to evaluate the nature of contact relationships between the crystalline pre-rift basement (Precambrian igneous and metamorphic rocks) and the *syn*-rift deposits. In general, the field observations were aimed at assessing the nature of intra-rift deformation along the rift basins.

3.2. Gravity data

To understand the geodynamic controls on the field-observed and remotely sensed structural deformation, we investigate the physical characteristics of the crust beneath the Albertine and Edward-George rift zones. More specifically, as part of the DRIAR Project, we acquired new ground-based gravity data and have combined them with existing public-domain terrestrial gravity data from the International Gravimetric Bureau (BGI) database (https://bgi.obs-mip.fr/data-products/gravity-databases/land-gravity-data-prod/#/data/land) (Balmino et al., 2012; Bonvalot et al., 2012) to image the bulk density structure of the crust beneath the rift zones. We acquired 1150-line kilometers of ground gravity data along eight profiles in Uganda with a line spacing of 1 km (profiles P1 to P8; Fig. 4A). We also compiled existing ground gravity data in Uganda, Kenya, and Congo, which include a dense network of gravity data collected in 5 main petroleum Exploration Areas (EA) in Uganda (see the locations of EA1 to EA5 in Fig. S1). We also obtained 6516 ground gravity data points from the International Gravimetric Bureau (BGI; Fig. S1A). Following Telford et al. (1990), we applied several corrections to the observed land gravity field (g_{obs}), including correction for the latitude (δg_L), free-air correction (δg_F), terrain correction (δg_T) using topographic heights from the SRTM-Digital Elevation Model and those obtained with our differential GPS instrument, and Bouguer correction (δg_B) using an average crustal density of 2670 kg m^{-3} and water density of 1030 kg m^{-3} to get the complete Bouguer Anomalies (∇g_B). The refined Bouguer anomaly is given by:

$$\nabla g_B = g_{obs} - \delta g_L + \delta g_F + \delta g_T - \delta g_B \quad (1)$$

We merged the Bouguer Anomalies from each of the datasets using the blend grid stitching method in the Grid-Knitting routine in Sequeent's Geosoft Oasis Montaj that interpolates the grid edges of the individual datasets to produce the compiled Bouguer Anomaly in Fig. S1B.

Since we are modeling the crustal and uppermost mantle structures, we have to correct for the gravity effect due to deeper mantle sources (i.e., at >120 km depths extending to the Core-Mantle Boundary). To make this correction, we use estimates of the gravity anomaly of the entire mantle beneath a ~ 120 km thick lithosphere that is benchmarked in ASPECT version 2.6.0-pre (Advanced Solver for Planetary Evolution, Convection, and Tectonics; Heister et al., 2017; Kronbichler et al., 2012; Bangerth et al., 2023a, 2023b; Clevenger and Heister, 2021; Gassmöller et al., 2020). This deep mantle gravity is obtained by scaling the S40RTS global seismic tomography model (Ritsema et al., 2011) into equivalent deep mantle density anomalies $\rho(\boldsymbol{r'})$ using a velocity-to-density scaling factor of 0.15 (e.g., Behn et al., 2004; Conrad et al., 2007; Conrad and Behn, 2010). The gravity anomaly $g(\boldsymbol{r})$ of the deep mantle is forward calculated from the deep mantle density anomalies $\rho(\boldsymbol{r'})$ using the Gauss-Legendre Quadrature (GLQ) elemental integration (Eq. 2, e.g., Asgharzadeh et al., 2007; Uieda and Barbosa, 2016, 2017).

$$g(\boldsymbol{r}) = \iiint_{\Omega} \frac{G\rho(\boldsymbol{r'})}{|\boldsymbol{r}-\boldsymbol{r'}|^2} d\boldsymbol{r'} = \sum_{k} \iiint_{\Omega_k} \frac{G\rho(\boldsymbol{r'})}{|\boldsymbol{r}-\boldsymbol{r'}|^2} d\boldsymbol{r'} \qquad \text{in} \quad \Omega_k \quad (2)$$

where $\boldsymbol{r}$, $\boldsymbol{r'}$ = radial distances from Earth's center to observation points in the mantle and a point source, respectively. $G = 6.67430 \times 10^{-11}$ $m^3/kg/s^2$ is the universal gravitational constant.

The resultant deep mantle gravity in Africa (Fig. S2A) indicates reasonable values (e.g., negative gravity anomalies) in well-known tectonic features such as the mid-Atlantic Ridge and the Eastern Branch of the East African Rift System, where hot mantle materials are present at shallow depths. Also, positive mantle gravity anomalies delineate the major cold cratons in Africa (Fig. S2A). The mantle gravity beneath the northern Western Branch (Fig. S2B) ranges between −67.6 and − 1.5 mGal, with lower values (−67.6 mGal to −4.5 mGal) occurring east of longitude 31° (Fig. S2B). We subtract the mantle gravity beneath the northern Western Branch (Fig. S2B) from the complete Bouguer Anomaly (Fig. S1B) to get the final mantle-corrected Bouguer Anomaly (Fig. 4A) that we use as input for our 3D gravity inversion and

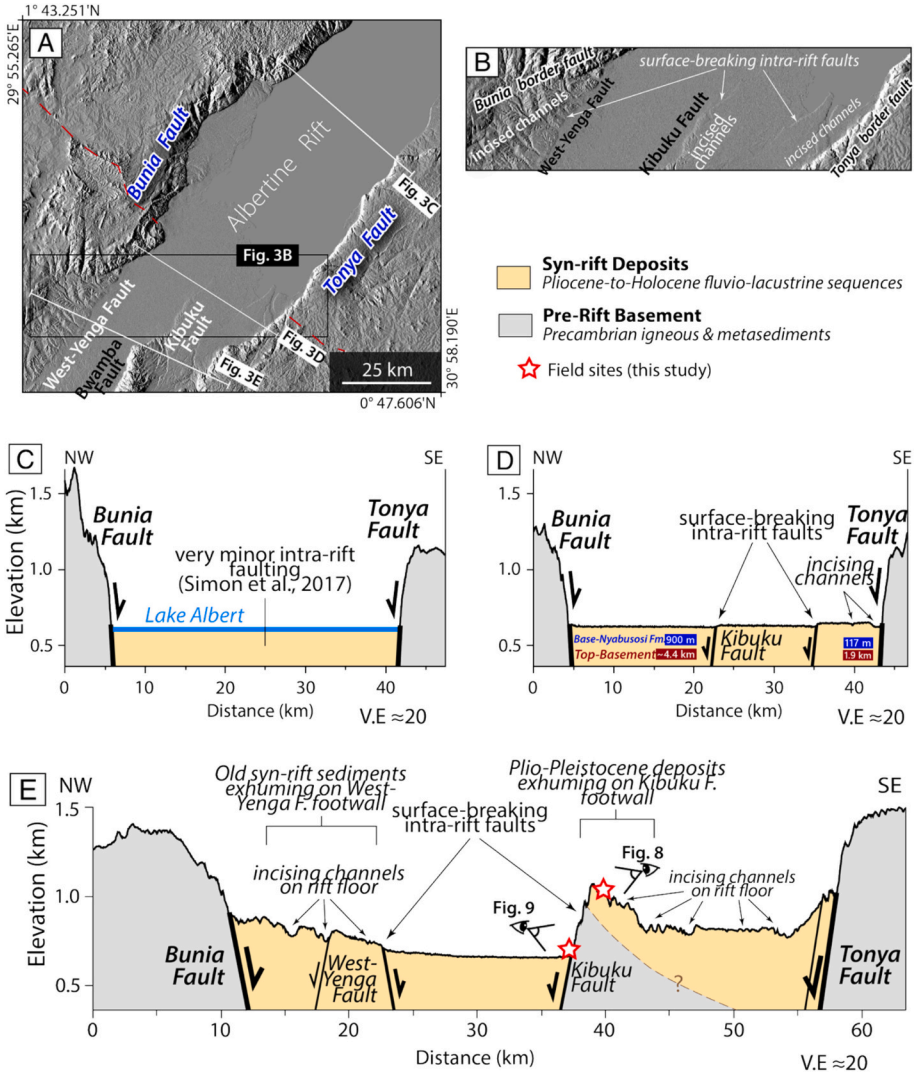

Fig. 3. **(A - B)** Topographic relief map of the magma-poor southern Albertine Rift, highlighting the presence of surface-breaking intra-rift fault scarps near the border faults and along the rift axis. The red-dashed lines in Fig. 3A represent the boundary between the Proterozoic basement of the Rwenzori Belt in the SW and the Archean cratonic basement of the Northeast Congo Block (Fig. 1B). **(C-E)** Topographic profiles across the southern Albertine Rift showing the relative magnitudes of rift-floor deformation along the prominent surface-breaking intra-rift faults. Along the profile in Fig. 3D, the depths to key horizons (early Pleistocene Base-Nyabusosi Fm, and Pre-rift basement) on one of the intra-rift faults are greater than those on the Tonya border fault (estimated from Simon et al., 2017). V.E = vertical exaggeration. Note that the illustrated fault dips in Figs. 3C-E are hypothetical and not measured. (For interpretation of the references to colour in this figure legend, the reader is referred to the web version of this article.)

2D forward modeling. The rift axis generally shows negative Bouguer Anomalies reaching ~ − 89 mGal (Fig. 4A), possibly due to the rifting activity or gravity anomalies due to the presence of uncorrected sedimentary cover. The Bouguer Anomalies (Fig. 4A) are lower in the AG than in the EGR, probably due to the presence of thicker sediments beneath Lake Albert compared to those beneath Lake Edward (i.e., ~5 km versus 4.5 km, respectively; Upcott et al., 1996).

We, however, test the effect of correcting for the deep mantle gravity by comparing results of the 3D gravity inversion of the mantle-corrected Bouguer Anomalies (Fig. 4A) with results from 3D inversion of the complete Bouguer gravity anomalies (Fig. S1B), which do not incorporate the mantle correction. See Fig. S3 in the supplement.

3.3. 3D gravity inversion

We use the code jif3D (Moorkamp et al., 2011) to perform 3D inversion of the gravity data using a deterministic inversion method that requires a smaller number of forward calculations when compared to stochastic inversion methods. Jif3D is a 3D multi-physics inversion framework for seismic, magnetotelluric (MT), and scalar and full tensor gravity data with capabilities to perform standalone inversion of the individual dataset (Moorkamp et al., 2011). It employs an iterative nonlinear optimization method based on a limited memory quasi-Newton method (L-BFGS) (Avdeeva and Avdeev, 2006) and a massively parallel implementation for the gravity forward problem (Moorkamp et al., 2010). Our density model domain has dimensions of ~702 x ~ 547 km in the easting (x) and northing (y) directions, respectively, and extends to a maximum depth of 150 km. We discretize the model into a mesh containing 64 × 64 × 30 cells, such that each cell is a rectangular prism with dimensions 11 × 8.5 × 5 km. The full objective function (Φ) that we minimize iteratively includes the data misfit term for the gravity anomaly data ($\Phi_{d,grav}$) and the regularization term ($\Phi_{reg,\rho}$):

$$\Phi = \Phi_{d,grav} + \lambda\Phi_{reg,\rho} \quad (3)$$

The gravity data misfit ($\Phi_{d,grav}$) is defined as the ***L2*** norm of the data residuals weighted by the uncertainties (10 mGal; Njinju et al., 2023b). $\Phi_{reg,\rho}$ is the model regularization term, which stabilizes the inversion process to yield smooth and geologically meaningful results (Zhdanov,

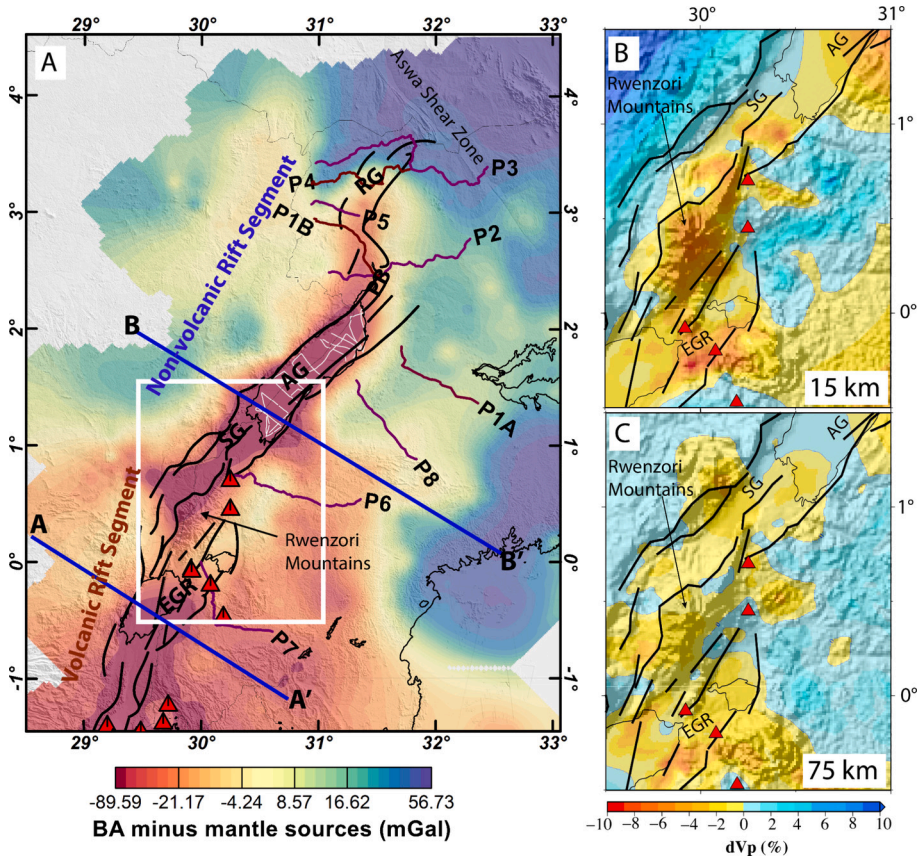

Fig. 4. (**A**) Ground Bouguer gravity anomaly minus deep mantle sources. The line paths labeled P1 to P8 are profile locations where we collected gravity data as part of the Dry-Rifting In the Albertine-Rhino graben (DRIAR) Project. The white line represents offshore gravity data collected during March and April 1992 through an NSF project in collaboration with the Ugandan Department of Geological Survey (Karner et al., 2000). The blue lines A-A' and B-B′ show the trace of the vertical (depth) sections of the density perturbations and 2D forward gravity models presented in Fig. 9. (**B**) Horizontal sections of P-velocity anomalies at depths of 15 km and 75 km (**C**) generated from the inversion of teleseismic events recorded by a temporal network of the RiftLink Project (Jakovlev et al., 2013). The white box represents the area shown in B and C. The black lines are faults from the Global Earthquake Model Foundation's (GEM) Global Active Faults Database (GAF-DB; Styron and Pagani, 2020). (For interpretation of the references to colour in this figure legend, the reader is referred to the web version of this article.)

2002; Njinju et al., 2023b). To achieve a smooth model, we define $\Phi_{reg,\rho}$ as the second spatial derivative of the density anomalies weighted by the individual a priori model covariance matrix, whose diagonal elements increase as the square of depth (Njinju et al., 2023b). λ is a scalar weight that controls the balance between the different terms of the objective function. We assume a starting model with zero density anomaly values everywhere, and the objective function is minimized by assigning new density anomaly values to each model cell (based on the forward numerical solution), and the density model is optimized iteratively until the misfit reaches a minimum or the user prescribed number of iterations is exhausted. The choice of the regularization parameter, λ, is guided by the analysis of trade-off curves or L-curves (Hansen, 1992). For the L-curve analysis, we ran 9 models with values of λ ranging from 10^2 to 10^6 (Table 1). We ran each model for 20 iterations and recorded the resultant RMS data misfit and corresponding model roughness (Table 1). We generate the L-curve by plotting the RMS data misfit versus the model roughness for the different regularization weights λ (Fig. 5). We find that the optimal parameterization for the gravity inversion that minimizes the data misfit and model roughness (kink or knee of the L-curve; Fig. 5) corresponds to $\lambda = 10^5$. We therefore chose $\lambda = 10^5$ and find that the model converges with acceptable RMS errors decreasing from 27.11 at the zeroth iteration to 1.79 at the 20th iteration (Table S1; Fig. 6A), producing a good fit between the observed Bouguer Anomaly (Fig. 6B) and the predicted Bouguer Anomaly (Fig. 6C) with data residuals within ± 4 mGal (Fig. 6D) that are less than the uncertainties (10 mGal) in the data.

Table 1
Regularization parameters for gravity inversion and the model statistics.

Gravity regularization weights, λ	RMS data misfit	Model roughness
100	1.54	1.77
500	1.54	1.76
1000	1.54	1.76
5000	1.55	1.73
10,000	1.55	1.69
50,000	1.63	1.46
100,000	1.79	1.27
500,000	3.45	0.66
1000,000	4.54	0.49

3.4. 2D forward gravity modeling

The 3D gravity model output by jif3D includes massive blocks of negative or positive density anomalies that are independent of geological layering (e.g., Paulatto et al., 2019; Lösing et al., 2023; Lowe et al., 2024), making it difficult to separate contributions from different parts of the crust and mantle. To validate the 3D inversion models and provide constraints on the density distributions of the different crustal layers and the uppermost mantle, we perform 2D forward modeling of the gravity data along profiles A-A′ and B-B′ (see Fig. 4A for profile locations). We use seismic constraints of crustal thickness from Wölbern et al. (2010, 2012) and Gummert et al. (2016). Findings from studies by Wölbern et al. (2010, 2012) and Gummert et al. (2016) indicate a thinner crust (~26 km) beneath the EGR and a thicker crust (~34 km) beneath the rift

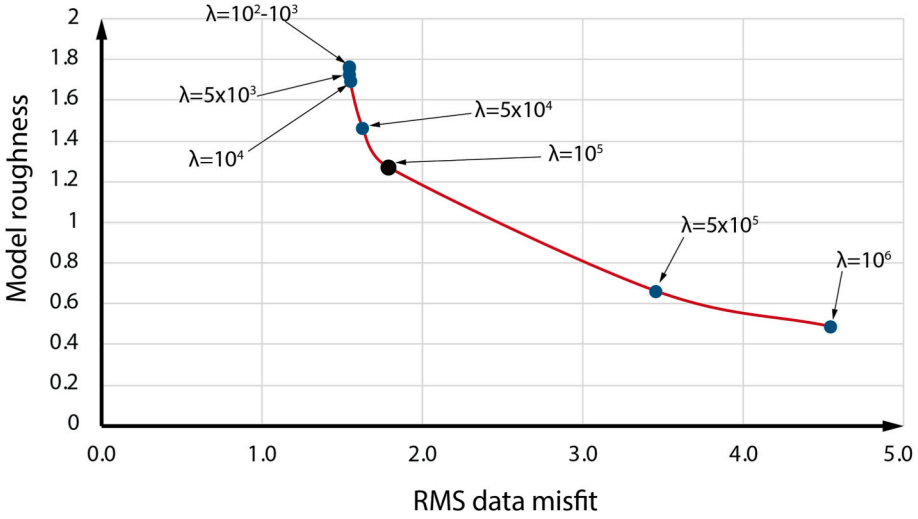

Fig. 5. L-curve (trade-off curve) for the gravity inversion models indicating the regularization parameter values, λ, used. λ $=10^5$ is the optimal regularization parameter that minimizes the model roughness and the data misfit (black circle).

shoulders. Additionally, seismic tomography studies by Jakovlev et al. (2013) indicate low-velocity zones beneath the EGR and the Toro-Ankole volcanic fields, extending beneath the Rwenzori Mountains into the southern tip of the ARG at depths of ~15 to 80 km (Figs. 4B and C). We determine the final gravity model by varying the initial crustal thickness from Wölbern et al. (2010, 2012) and Gummert et al. (2016) by ~10 % and the initial densities of the different Earth layers estimated from East African Rift gravity models (e.g., Fletcher et al., 2018; Leseane et al., 2015; Mickus et al., 2007; Njinju, 2016; Njinju et al., 2019a; Njinju and Atekwana, 2025; Nyalugwe et al., 2019; Simiyu and Keller, 2001) by ~15 % to fit the predicted and the observed gravity data.

In our 2D forward modeling, we also examine the contribution of sediments to the observed gravity anomalies beneath the Lake Edward Basin and the Albertine Graben (Lake Albert) using sedimentary thickness constraints from both basins. The sedimentary thickness in the Lake Edward Basin reaches ~4.5 km and < 1.5 km beneath Lake George based on estimates from Werner and Euler deconvolutions of gravity and magnetic data (Upcott et al., 1996), which also shows that the main depocenter of Lake Edward is located on the north-eastern shore. Seismic reflection and gravity studies results indicate sedimentary thickness reaching ~5 km in the Albertine Graben with the main depocenter along the Bunia Fault (Karp et al., 2012). In the southern portion of the ARG (transected by profile BB'; Fig. 2A), the southernmost depocenter is located on the hanging wall of the Tonya Fault (Karp et al., 2012; Simon et al., 2017).

4. Results

4.1. Field observations of intra-rift faulting in the Lake George Rift

The rift floor of the Lake George Rift is characterized by broad plains of gently rolling undulations, except for locations where they are punctuated by 1–2 km-wide spherical depressions representing volcanic craters (Fig. 7A). In many places, we find that abrupt gradients in these slopes of the rolling hills correspond to fault traces that are observable on elevation models and satellite imagery (Figs. 7B-C). Also, the abrupt gradients are commonly collocated with vegetation gradients where lush vegetation is hosted in the downthrown side and sparse vegetation on the upthrown side (e.g., Figs. 7D-E), consistent with previously published structural observations in satellite imagery (Wedmore et al., 2024). However, there are other cases where the fault traces are not collocated with vegetation gradients (e.g., Fig. 7F). Overall, we note that the topographic relief across the fault scarps is commonly <10 m high, and we do not observe the presence of any slip surface along the scarps. Similarly, the topographic relief approaching the volcanic craters is subdued within the rift floor (e.g., Fig. 7G) but is prominent and steeper along the border fault (see background of Fig. 7A and G).

4.2. Field observations of intra-rift faulting in the southern Albertine Rift

Unlike the Lake George Rift, where small topographic offsets and an absence of exhumed basement rocks characterize the intra-rift fault traces, the Kibuku Fault, which is the most prominent intra-rift fault of the southern Albertine Rift (north of Semiliki Graben), hosts exhumed fluvio-lacustrine *syn*-rift sequences of cross-bedded siltstones and sandstones of the Early Pleistocene Nyabusosi Formation and Late Pleistocene Rwebishengo Beds (Figs. 8 A-C). The earlier syn-rift sequences are exposed on the Kibuku Fault escarpment, at the base of which are the Precambrian granitic basement exposures hosting the fault slip surfaces (Fig. 9A). The exhumed sediments are tilted eastwards (Figs. 8 A-B) and are reworked by incising channels into the subsiding hanging wall of the Kibuku Fault and that of the Tonya Fault (Fig. 3A and E). At the base of the escarpment, the slip surface of the Kibuku Fault is characterized by stacks of breccia sheets with quartz gouge and well-preserved slickenlines (Figs. 9A-C). We observe quartz and gypsum geochemical cementing of the fractured lower section of the sandstones and the adjacent granitic basement fault block. Altogether, the rift axis of the southern Albertine Rift hosts pronounced high-offset basement-rooted faults with prominent geochemical alterations on slip surfaces, which are lacking in the field exposures of the intra-rift faults of the Lake George Rift. The anomalous footwall uplift event on the Kibuku Fault exposing older syn-rift deposits (Fig. 3E) and field evidence of geochemical alterations in the fault rocks suggest possible control of deeper crustal processes.

4.3. Along-axis variability of density anomalies beneath the rift segments

We observed negative density anomalies of ~ − 60 to −20 kg/m^3 extending from the surface to depths of ~50 km and ~ −20 to −1 kg/m^3 within depths of ~50–100 km beneath both the magma-rich EGR and the magma-poor ARG compared to positive density anomalies (~0 to 60 kg/m^3) in the rift shoulders and surrounding cratons (Figs. 10A and B). In the ARG, negative density anomalies are more focused beneath the rift axis, with the lowest values occurring in the Albertine Graben (~ − 60 kg/m^3) extending beneath the Semliki Graben and the Rwenzori Mountains to the EGR (Figs. 10A and B). There are blocks with positive

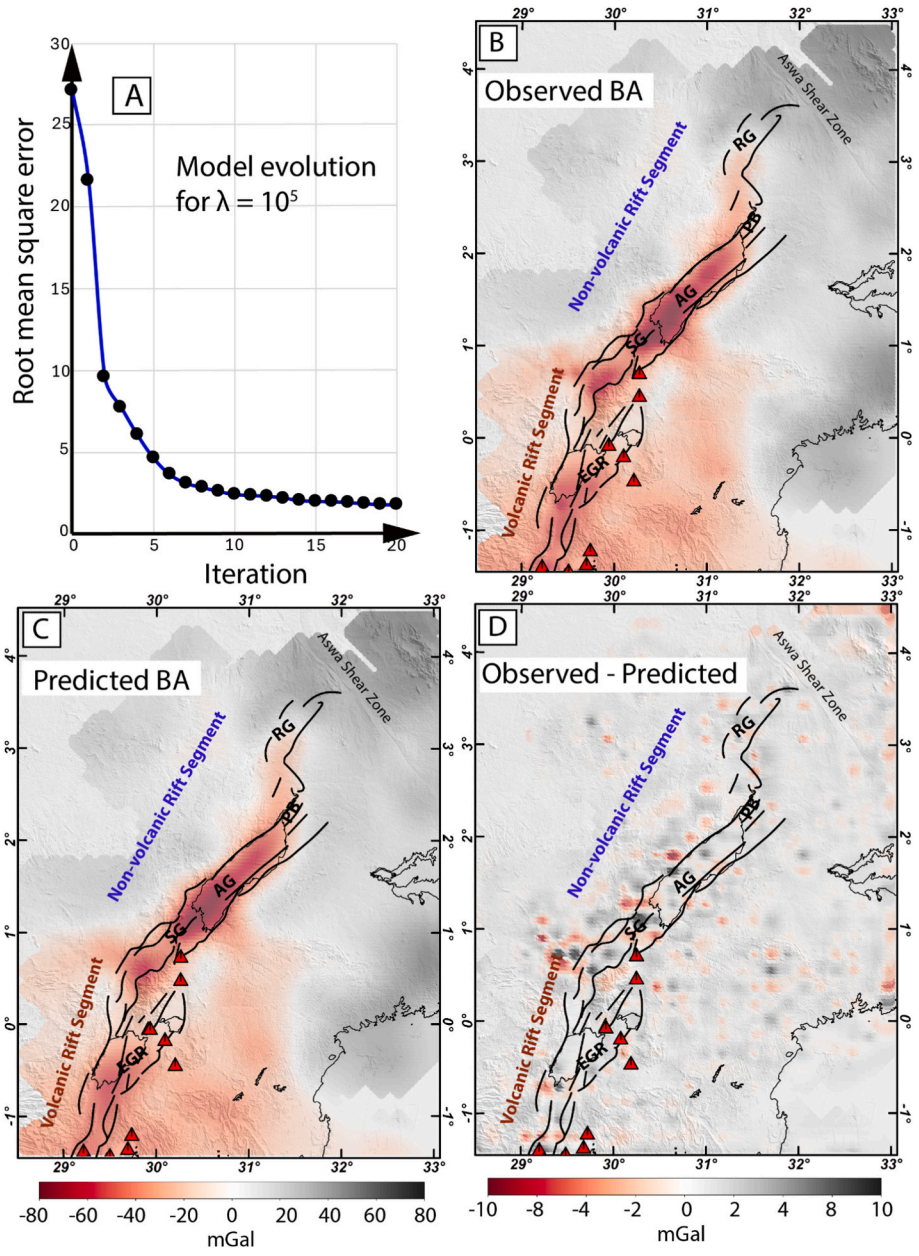

Fig. 6. (**A**) Root mean square error between observed and inverted gravity field for each inversion iteration. (**B**) Gravity inversion input data (here called Observed Bouguer Anomaly), which is the ground Bouguer gravity anomaly minus deep mantle sources. (**C**) The predicted gravity calculated from our resultant density anomaly. Fig. 6B and C share the same colorbar. (**D**) Residual gravity, which is the difference between the observed (Fig. 6B) and the predicted (Fig. 6C) gravity anomalies, showing a good fit between the predicted and observed gravity data. The black lines are faults from the Global Earthquake Model Foundation's (GEM) Global Active Faults Database (GAF-DB; Styron and Pagani, 2020). The red triangles are Holocene volcanoes of the Toro-Ankole Volcanic Province (TAVP) obtained from the Global Volcanism Program (2023). EGR = Lakes Edward-George Rift. SG = Semliki Graben. AG = Albertine Graben. PB = Pakwach Basin. RG = Rhino Graben. (For interpretation of the references to colour in this figure legend, the reader is referred to the web version of this article.)

density perturbations (~20 kg/m^3) on both the western and eastern flanks of the Rwenzori Mountains that extend from shallower depths to depths <50 km (Figs. 10A, B, and C). At depths >50 km, the region of lower density anomaly (~ − 10 kg/m^3) is wider beneath the magma-rich EGR and narrows northward beneath the non-volcanic ARG (Fig. 10D). Our results show that significant portions of the negative density anomalies are shallower than <50 km and thus within the crust and the uppermost mantle with even lower density anomalies within the lower-crust at depths between 15 and 20 km (Figs. 10 A and B).

4.4. 2D forward gravity model of the rift segments

The depth section of our inverted density anomalies along the magmatic EGR (see profile AA' in Fig. 2A) shows negative density perturbations beneath the EGR that are focused beneath the Lake Edward Basin at depths generally <30 km and sandwiched between fragments with positive density perturbations (Figs. 11A and B). This region with negative density perturbations has a corresponding gravity minimum (−60 mGal; Fig. 11C). Results from the 2D forward model (Fig. 11D) relative to the surrounding crustal layers show a low-density upper-crust (2.6 g/cm^3), a low-density lower-crust (2.7 g/cm^3) and a low-density mantle (3.2 g/cm^3) underlying the region of thinned crust (~22 km)

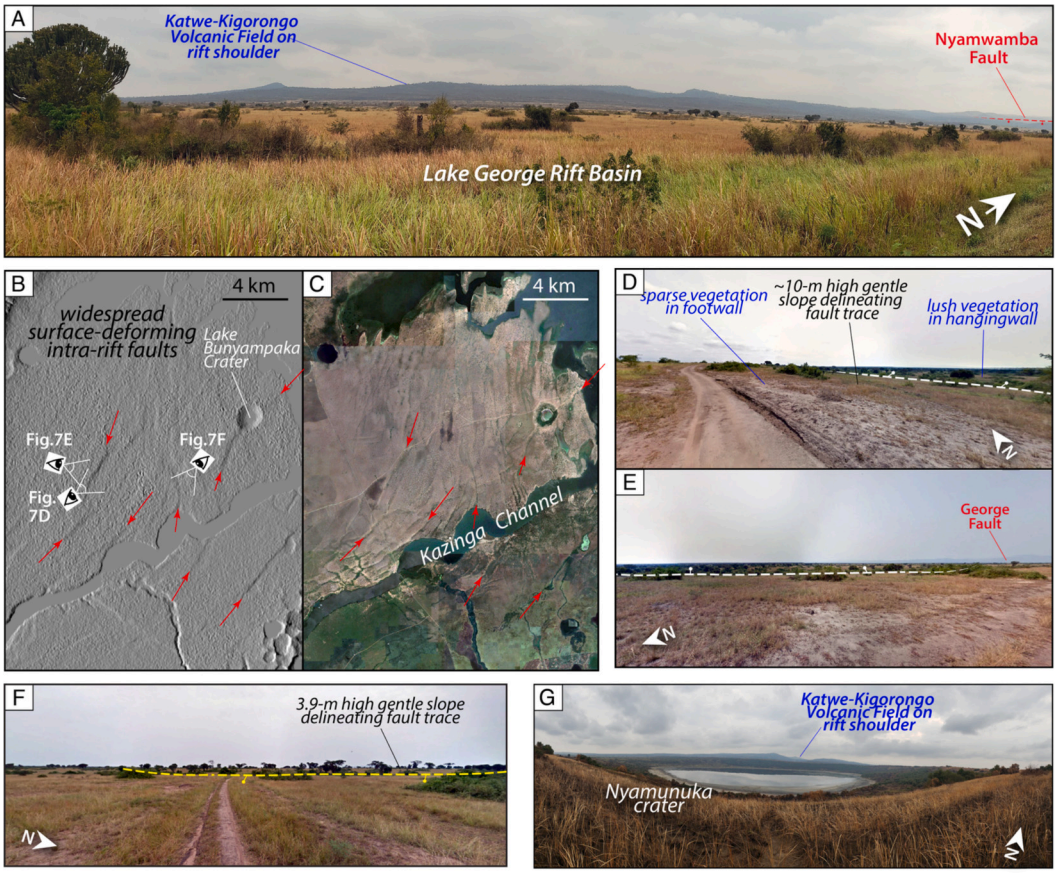

Fig. 7. (**A**) Field photograph showing the typical 'flat' relief landscapes of the rift floor along the axis of the Lake George Rift, particularly away from the intra-rift magmatic centers. (**B**) Topographic field map (Shuttle Radar Topo. Mission, SRTM) and (**C**) satellite imagery (source: Google Earth) showing widespread distributed rectilinear and curvilinear scarps collocated with vegetation gradients along the axis of the Lake George Rift. Note how the scarps offset one of the intra-rift volcanic centers (Bunyampaka Crater). (**D - F**) Gentle, <10-m high scarp that is collocated with lush vegetation on the downthrown surface and contrasting sparse vegetation on the upthrown surface. These three photos were obtained from Google Street View. (**G**) Panoramic field photograph showing the Nyamunuka Crater on the hanging wall of the Nyamwamba border fault and other clustered craters of the Katwe-Kigorongo Volcanic Field on the uplifted rift shoulder (see Fig. 2A for location of the craters).

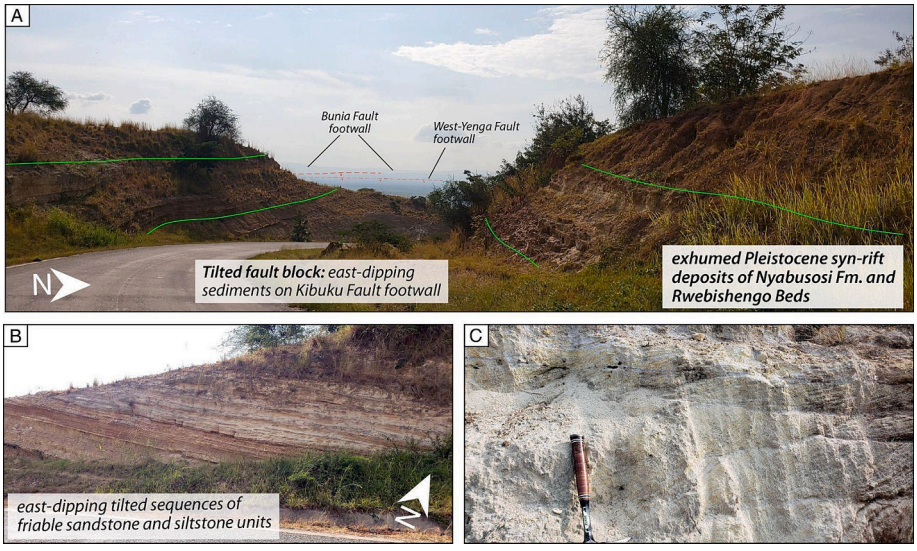

Fig. 8. (**A - C**) Field photographs (looking west in panel A) showing tilted exhumed earlier syn-rift fluvio-lacustrine deposits (Early Pleistocene Nyabusosi Formation and Late Pleistocene Rwebishengo Beds; Pickford et al., 1993; Roller et al., 2010), exhumed on the footwall of the Kibuku Fault. The units are east-dipping and are composed of friable, poorly consolidated sandstones and claystones.

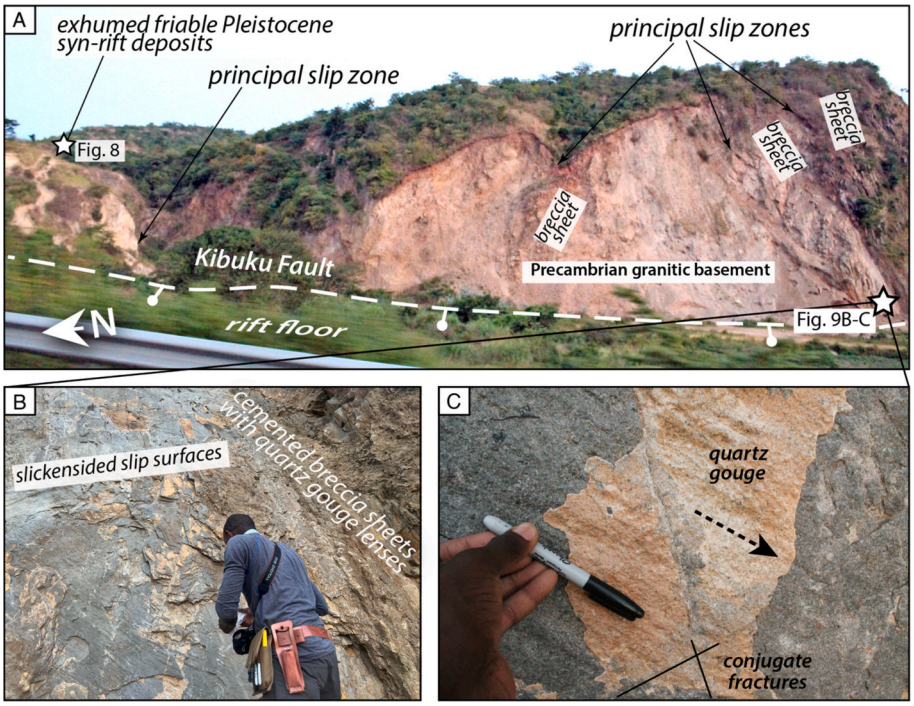

Fig. 9. Field photograph (looking east) of (**A**) the Kibuku Fault escarpment (with active quarry) along the rift axis, and (**B - C**). The basement-rooting principal slip surface of the Kibuku intra-rift fault, exhibiting geochemical alterations of the fault zones by silica and gypsum. The silicified slip surfaces preserve excellent oblique-normal striae on the quartz gouge lenses.

beneath the EGR. Similarly, the depth section along the non-volcanic ARG (see profile BB' in Fig. 4A) shows that the most negative density perturbations are focused beneath the Albertine Graben (Lake Albert) at depths generally <50 km with a sharp transition to positive density perturbations in the western rift flank (Fig. 11E and F). This region with negative density perturbations also has a corresponding gravity minimum (−80 mGal; Fig. 11G). Results from the 2D forward model (Fig. 11H) show a low-density upper-crust (2.6 g/cm^3), a low-density lower-crust (2.7 g/cm^3), and a low-density mantle (3.2 g/cm^3) underlying the region of thinned crust (~28 km) beneath the Albertine Graben. However, the lower-crust beneath the EGR is more significantly stretched (Fig. 11D) compared to the lower-crust beneath the ARG (Fig. 11H).

5. Discussion

5.1. Fluid-assisted crustal deformation in the non-volcanic southern Albertine Rift

Field observations and examination of topographic relief show that the southern Albertine Rift exhibits pronounced intra-rift tectonic faulting (Figs. 3, 8–9) that is anomalous for juvenile magma-poor continental rifts, and potentially reflects the control of deeper crustal/lithospheric processes (e.g., Muirhead et al., 2019). Although the rift exhibits the greatest throw on its border faults, similar to the magma-rich volcanic Lake George Rift, there is a clear distinction in the prominence of intra-rift faulting and magnitude of the accrued displacement on the faults. The Lake George Rift manifests intra-rift crustal deformation in the form of distributed small offset faults and magmatic structures (cinder cone eruption vents) (Figs. 2 and 7), whereas, in the southern Albertine Rift, the deformation manifests in the form of a few but prominent higher-offset intra-rift faults (Fig. 3D-E and 9). More importantly, progressive slip on the most prominent intra-rift fault in the southern Albertine Rift, the Kibuku Fault, has exhumed the Early-to-Late Pleistocene (and Pliocene?) *syn*-rift deposits and the underlying pre-rift basement in its footwall (Figs. 3E, 8), indicating that the acceleration of slip on the fault is likely Late-/Post-Pleistocene, ensuing much later after the rift initiation and establishment of the border faults. Observations from crustal desnsity and seismic velocity distributions (Figure 10 and 11) lead us to speculate that the tiggering of accelerated slip on the Kibuku Fault may be associated with an an event of increased buoyancy of the crust (de-densification) from the infiltration of mantle-derived fluids into the lower-crust. This mantle fluid infiltration could have been accompanied by thermal perturbation of the lithosphere, and with fluid pressurization producing a decrease in effective normal stresses at depth.

The contrasts in the physics of crustal stretching between evolving magma-rich and magma-poor rifts are manifested in the patterns of tectonic faulting in the two rift settings, particularly in the prominence of intra-rift accommodation of extension relative to border fault-dominated extension or lack thereof (Muirhead et al., 2019). Studies on early-rift focusing of intra-rift faulting in non-volcanic rifts suggest that this may be influenced by either: (1) inherited crustal- and lithospheric-scale shear zones acting as mechanical zones of weakness (Kolawole et al., 2021a), (2) a lower-crustal weak layer (Wedmore et al., 2024), (3) rift tip splays from a propagating rift tip into the axis of an adjacent interacting rift pair (Kolawole et al., 2021b; Njinju et al., 2025), or (4) rift-axial melt lenses in the lower-crust (Ajala et al., 2024). The focusing of tectonic strain on the Kibuku Fault cannot be explained solely as a by-product of the uplift of the Rwenzori Mountains since the Kibuku Fault is a side-step fault to the northeast of the Bwamba Fault (west-bounding fault of the Rwenzori Block; Fig. 3A). Although the two faults are now hard-linked, they most likely developed independently. The Kibuku Fault represents the west-bounding fault of a narrow horst (bounded to the east by the Rwimi Wasa Fault) that extends northeast from the northern end of the main Rwenzori Block (Fig. 3A). Structural studies of the neotectonics of the Rwenzori Mountains suggest that the large crustal uplift may have accommodated lateral block rotation, given by field observations of strong strike-slip faulting (Koehn et al., 2008; Sachau et al., 2016). This strike-slip kinematics does not seem to be compatible with dominant oblique dip-slip displacement vectors on the Kibuku Fault slip surface exposures (Fig. 9C).

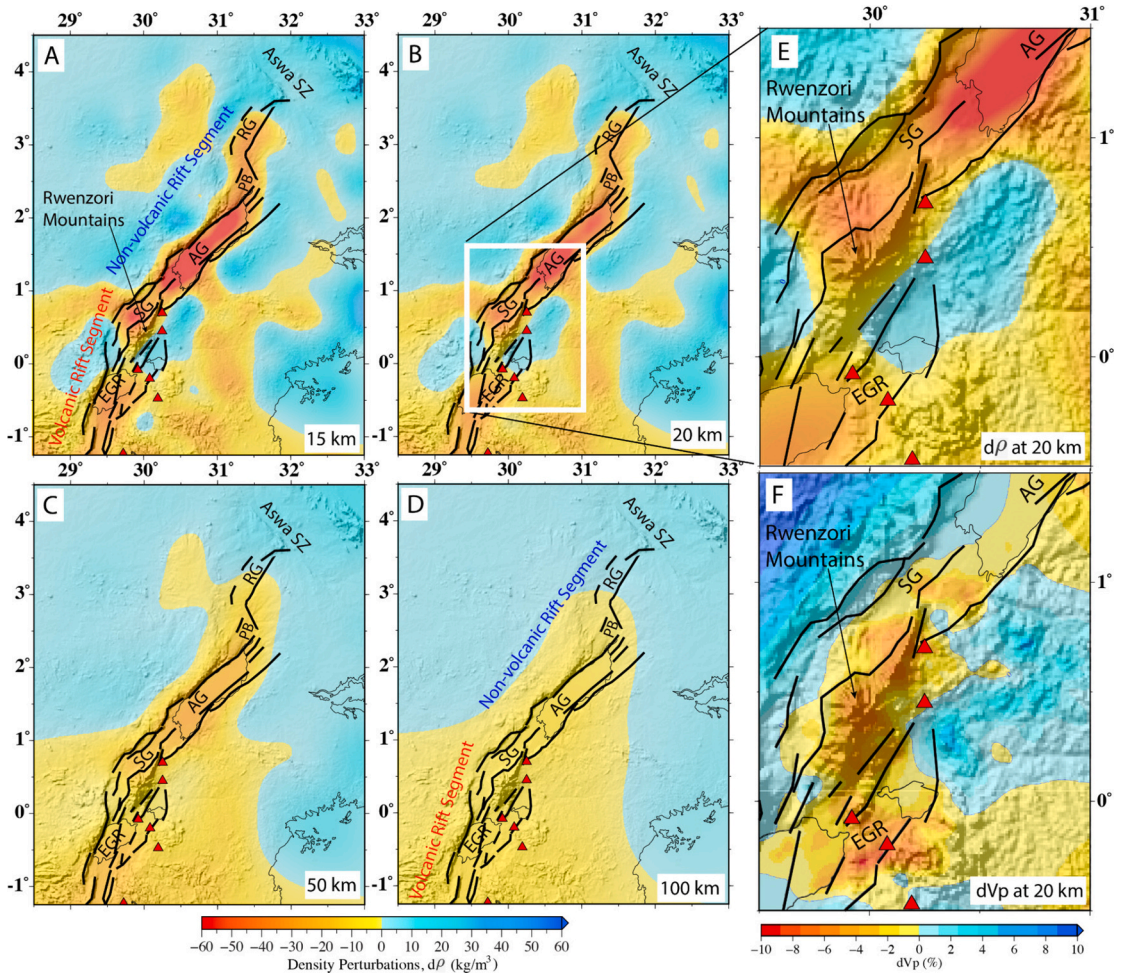

Fig. 10. (**A**) Density perturbations beneath the northern Western Branch of the EARS at depths of 15 km, 20 km (**B**), 50 km (**C**), and 100 km (**D**). (**E**) The density perturbations at 20 km for the region of study for the RiftLink Project (white box in A; Jakovlev et al., 2013). (**F**) Horizontal sections of P-velocity anomalies at depths of 20 km (Jakovlev et al., 2013). The black lines are faults from the Global Earthquake Model Foundation's (GEM) Global Active Faults Database (GAF-DB; Styron and Pagani, 2020). The red triangles are Holocene volcanoes of the Toro-Ankole Volcanic Province (TAVP) obtained from the Global Volcanism Program (2023). EGR = Lakes Edward-George Rift. SG = Semliki Graben. AG = Albertine Graben. PB = Pakwach Basin. RG = Rhino Graben. (For interpretation of the references to colour in this figure legend, the reader is referred to the web version of this article.)

Accelerated Quaternary intra-rift faulting in the southern Albertine Rift is independent of uplift initiation in the Rwenzori Block. Cenozoic uplift of the Rwenzori initiated at ~2.7 Ma, at least 4 million years after initiation of Cenozoic tectonic extension (Pickford et al., 1993; Simon et al., 2017). Uplift rates across the Rwenzori indicate that crustal exhumation cannot be explained by displacement accrual and footwall flexure on the faults that bound the Rwenzori (Nyamwamba Fault to the SE and Bwamba Fault to the NW), highlighting that the dynamic uplift of the Rwenzori Block was induced by mantle processes (Wallner and Schmeling, 2010; Xue et al., 2017). Furthermore, seismic imaging shows thinned crust and rift-parallel mantle seismic anisotropy beneath the Rwenzori (Homuth et al., 2016; Wölbern et al., 2010). Considering that the youngest exhumed syn-rift sediments on the Kibuku Fault footwall are the Late Pleistocene Rwebishengo Beds (Fig. 8; Pickford et al., 1993; Roller et al., 2010), we argue that the acceleration of slip on the Kibuku Fault initiated in the Late Pleistocene, corresponding to the Albertine 'rift phase 2' of Simon et al. (2017). Altogether, these findings support the hypothesis that the accelerated intra-rift faulting event in the southern Albertine Rift in the Late Pleistocene may be due to an increase in crustal buoyancy, possibly related to tectono-thermal events in the lower-crust and lithospheric mantle. To understand the possible control of crustal buoyancy on anomalous intra-rift deformation, we assess the density structure of the crust and uppermost mantle beneath the Albertine Rift and evaluate the variability of the structure with that of the magma-rich southern continuation of the rift system in the Lake George Rift, using potential fields and seismological data.

5.2. *Crustal density perturbations beneath the non-volcanic Southern Albertine and volcanic Lake George rifts*

We compare the distribution of density anomalies at 20 km depth (Fig. 10E) with the distribution of P-wave velocity anomalies at a similar depth (Fig. 10F), provided by Jakovlev et al. (2013). Regions with negative density perturbations (Fig. 10E) (i.e., the region beneath the Albertine Graben that extends beneath the Semliki Graben and the Rwenzori Mountains into the EGR and the Toro-Ankole Volcanic Province) have corresponding negative P-wave velocity anomalies (Fig. 8F; Jakovlev et al., 2013). Similarly, the region with positive density anomalies in the eastern flank of the Rwenzori Mountains (Fig. 10E) has corresponding positive P-wave velocity anomalies (Fig. 10F). The close comparison of our resultant density anomalies (Fig. 10E) and the P-wave velocity anomalies (Fig. 10F; Jakovlev et al., 2013) indicates that both anomalies have the same causative source.

Our 2D forward models are used to suggest that the gravity minima beneath both the magma-rich EGR and the non-volcanic ARG (i.e., −60 mGal and − 80 mGal, respectively), and thus their corresponding

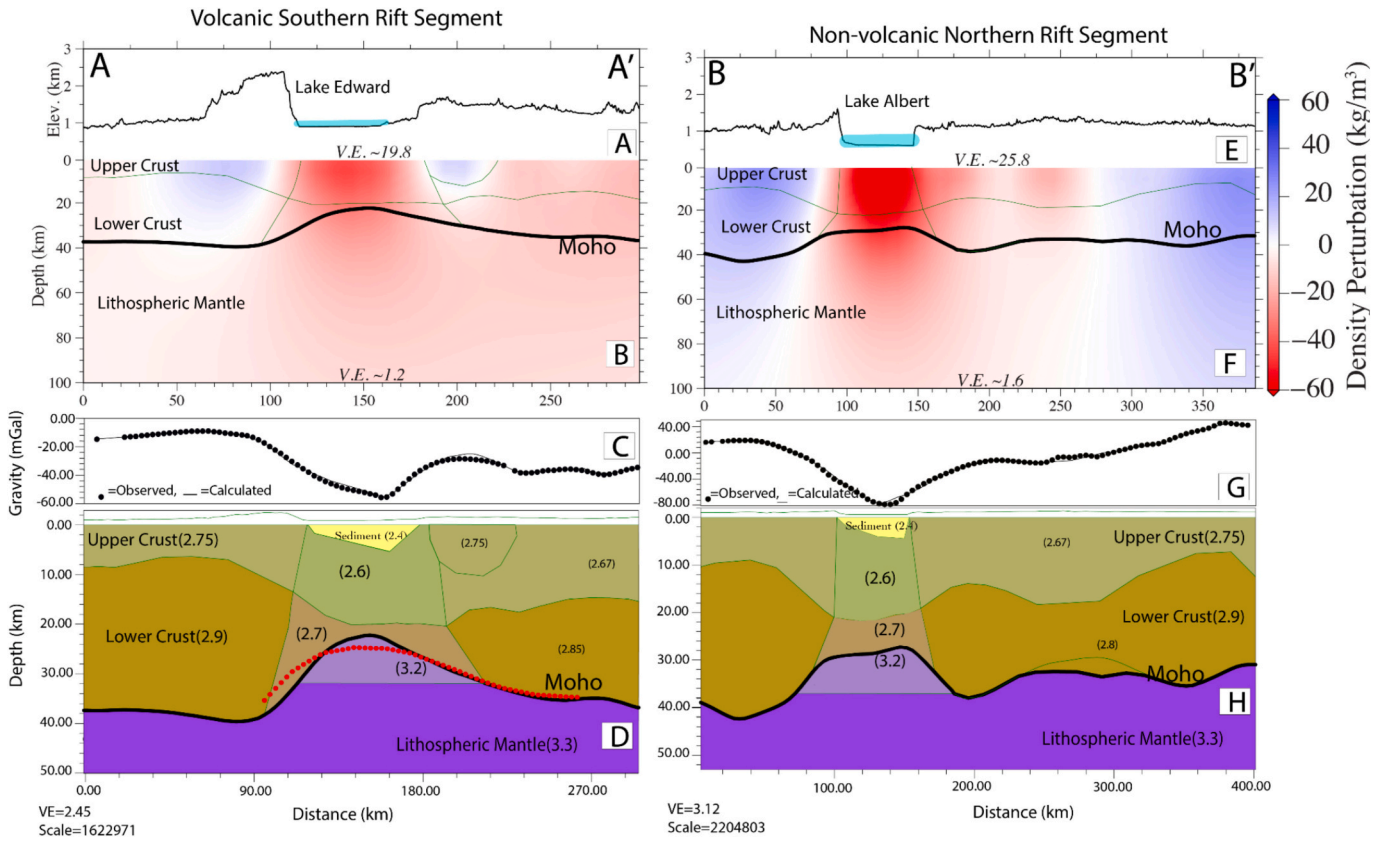

Fig. 11. Cross sections of profile lines in Fig. 3D. (**A**) Elevation along profile A-A'. (**B**) Density perturbations. (**C**) Observed (black dots) and calculated (thin black line) Bouguer gravity anomalies from two-dimensional forward modeling. (**D**) Interpretation of gravity forward modeling. (**E**), (**F**), (**G**), and (**H**) are the same as (A), (B), (C), and (D), respectively, but for profile B-B′ (see blue profile lines A-A' and B-B′ in Fig. 2A). The values in (D) and (H) are densities in g/cm^3. The Moho depths in (D; thick black line) are constrained by the extrapolated seismic receiver function Moho estimates (red dots) from the RiftLink Project (Gummert et al., 2016; Wölbern et al., 2010). (For interpretation of the references to colour in this figure legend, the reader is referred to the web version of this article.)

negative density anomalies cannot be explained by their thick sedimentary cover alone. Part of the gravity minima could be caused by a low-density region in the lower-crust and/or uppermost mantle where the densities should be at least 5 % lower than the surrounding regions. The exact placement of the low-density region cannot be determined by gravity modeling alone. However, seismic tomography constraints (Jakovlev et al., 2013) and the distribution of seismicity (Lindenfeld et al., 2012) indicate melt inclusion in the crust and uppermost mantle, which suggests that this low-density body, extending to the uppermost mantle, is due to the presence of melt.

The 2D forward model for the EGR (Fig. 11D) indicates that the crust is thinnest beneath the rift axis (~22 km) and thicker beneath the rift shoulders (~38 km), which can be explained by a crustal stretching factor of ~1.7 (i.e., 38/22 = 1.7) versus ~1.3 (i.e., 34/26 = 1.3) based on seismic receiver function estimates (Wölbern et al., 2010, 2012; Gummert et al., 2016). Similarly, the 2D forward model for the Albertine Graben (Fig. 11H) indicates that the crust is thinnest beneath the rift axis (~28 km) and thicker beneath the rift shoulders (~38 km), consistent with a stretching factor of ~1.3 in the ARG. Comparing the stretching factors for the EGR (i.e., ~1.3–1.7) and the AGR (i.e., ~1.3) indicates that there is a greater propensity for decompression and easier upward migration of deeper melt sources due to a larger pressure gradient in the EGR than in the ARG. Numerical simulation by Armitage et al. (2018) suggests that crustal stretching can influence melt generation in the asthenosphere, such that the thickness of melt generated increases sigmoidally with crustal stretching. Thus, a large part of the negative density perturbations in the EGR are due to the presence of melt in the lower-crust and/or uppermost mantle infiltrated from deeper sources. Earlier studies of the EGR indicate significant thinning of the crust beneath the rift axis (Wölbern et al., 2010; Gummert et al., 2016) and low P-wave velocity zones, which were used to suggest the presence of melt infiltration beneath the EGR, the Toro-Ankole Volcanic Province, and the Semliki Graben (Jakovlev et al., 2013). Further support for magma-assisted rifting in the EGR comes from magnetotellurics (MT) investigations, which show a conductive crustal anomaly beneath the Toro-Ankole Volcanic Province (Häuserer and Junge, 2011). Additionally, a study of seismic swarms by Lindenfeld et al. (2012) was used to suggest vertical melt/and or CO_2 migration within fault systems from a magmatic source within the lithosphere.

We argue that ascending melts generated at the lithosphere-asthenosphere boundary of the upper mantle, due to decompression and possible partial melting in the lower-crust due to elevated geotherms, contribute to the reduction of the density of the ductile lower crust beneath the ARG. The northward narrowing of the negative density anomalies beneath the ARG suggests a northward decrease in the contribution of melt in lower crustal de-densification, which possibly explains why the RG is less developed compared to the AG. The reduction of lower crustal density due to the presence of melt is consistent with observations of 'blind melts' beneath another magma-poor, non-volcanic rift segment of the EARS (Ajala et al., 2024; Kolawole and Ajala, 2024; Njinju and Atekwana, 2025). The partial melting of the lower-crust, where it occurs, is driven by advection of heat into the lower-crust by upward ascent of melt from the lithosphere-asthenosphere boundary. Such a reduction in lower crustal density, along with thick sedimentary cover at the uppermost crust (Fig. 11H), explains the gravity-low and negative density anomaly beneath the magma-poor AGR. A lower crustal stretching factor of 1.3 indicates that partial melts in the lower-crust will be locked between

rock grain boundaries, as the pressure gradient beneath the less stretched crust is not high enough to allow upward migration of these melts to breach the surface. Melt transport in the crust is mainly controlled by pressure gradients, crustal properties such as its elasticity, yield strength, and porosity, and fluid properties such as viscosity and buoyancy (e.g., Phipps Morgan and Holtzman, 2005; Stuart et al., 2016). Additionally, the emplacement and trapping of melts in the uppermost mantle and lower-crust could advect and trap heat into the lower-crust, and along with an overall decrease in crustal strength and fluid-induced decrease in effective normal stresses, may have initiated accelerated fault slip in the rift axis. Elsewhere, in the northernmost segment of the Rio Grande Rift System, where progressive extension of the continental crust accommodates non-volcanic early-stage rift basins, studies have also reported the presence of widespread 'blind' partial melts in the lower-crust beneath the rift basins, evidenced by the magnetotelluric imaging (Feucht et al., 2017; Murphy et al., 2024). It has been shown via geodynamic models that small melt fractions beneath magma-poor rifts could promote strain localization in the lithosphere and aid progressive crustal and lithospheric extension (Buck, 2004; Bialas et al., 2010; Ajala et al., 2024). Numerical modeling by Bialas et al. (2010) suggests that for an 80 km thick section of continental lithosphere, the amount of magma needed for rifting is small, with a maximum cumulative dike opening of ~4 km in the mid- to upper crust, with substantially less opening in the hotter mantle regions. Similarly, in the Okavango Rift Zone, which is another magma-poor rift in the southwestern branch of the EARS, seismic imaging suggests that the crust beneath the rift axis is thinned, and seismic velocities in the crust indicate deep emplacement of low-density materials (Yu et al., 2015).

6. Conclusions

As part of the NSF-funded DRIAR project, we conducted field mapping of surface scarps observable on topographic maps of the contrasting rift structure between the magma-poor Albertine-Rhino Rift (ARG) and its contiguous magma-rich Edward-George Rift (EGR) to assess the nature of intra-rift crustal deformation along the juvenile rift basins. We hypothesize that an anomalous intra-rift deformation in the magma-poor segment is governed by deep crustal processes. To test this hypothesis, in addition to field mapping, we estimate the lithospheric density structure beneath the ARG and the EGR.

Our field observations indicate that the southern ARG exhibits prominent intra-rift strain via focused displacement accrual on a few faults, unlike the EGR, where distributed low-offset faulting and magmatic vents accommodate intra-rift strain. Our observations of exhumed age-constrained *syn*-rift sediments on the footwall of basement-rooted high-offset intra-rift faults in the southern ARG suggest a Late Pleistocene acceleration of intra-rift crustal deformation. We posit that this anomalous intra-rift crustal deformation is due to an increase in the crustal buoyancy (de-densification) resulting from the infiltration of mantle-derived hot fluids into the crust.

Gravity and seismological investigation of the crustal and uppermost mantle imaging of the rift zone indicates:

1. Crustal density from gravity inversion data shows negative density anomalies extending from the surface to the uppermost mantle beneath both EGR and the ARG, with even lower anomalies at depths <50 km beneath the Albertine Graben in the ARG. 2D forward gravity modeling indicates thinning and de-densification of the crust and uppermost mantle (due to partial melts) beneath both the EGR and the ARG, however, with greater crustal stretching factors in the EGR (~1.3–1.7) compared to a stretching factor of ~1.3 in the ARG.
2. Based on the crustal stretching factor estimates, we infer that the gravity minima and low-density anomalies beneath both the magma-rich EGR and the magma-poor AGR are partly due to partial melting and flow of the lower-crust.
3. Gravity minimum and negative density anomalies beneath the magma-poor ARG are largely due to thick sedimentary cover and partial melt-induced decrease in lower crustal density.

The tectonic extension and associated crustal deformation in non-volcanic rifts are likely aided by deep crustal melts that suffer from delayed surface breaching (i.e., blind magmatism) due to their limited melt volumes, and the fact that low-pressure gradients (due to limited stretching) associated with most magma-poor rifts further limit the upward migration of melt. Such trapping of ascending mantle melts could advect and trap heat into the lower-crust, and along with an overall decrease in crustal strength via fluid pressurization at depth, could accelerate slip on the intra-rift faults, thus promoting tectonic strain accommodation in the rift axis.

CRediT authorship contribution statement

Emmanuel A. Njinju: Writing – review & editing, Writing – original draft, Visualization, Validation, Software, Resources, Project administration, Methodology, Investigation, Formal analysis, Data curation, Conceptualization. **Folarin Kolawole:** Writing – review & editing, Writing – original draft, Visualization, Validation, Resources, Methodology, Investigation, Formal analysis, Data curation, Conceptualization. **Estella A. Atekwana:** Writing – review & editing, Writing – original draft, Visualization, Validation, Supervision, Software, Resources, Project administration, Methodology, Investigation, Funding acquisition, Conceptualization. **Rasheed Ajala:** Visualization, Validation, Software, Formal analysis. **Eliot A. Atekwana:** Writing – original draft, Supervision, Resources, Project administration, Funding acquisition. **D. Sarah Stamps:** Writing – original draft, Visualization, Validation, Supervision, Software, Resources, Project administration, Funding acquisition, Conceptualization. **Rob.L. Evans:** Writing – original draft, Supervision, Resources, Project administration, Funding acquisition, Conceptualization. **Andrew Katumwehe:** Writing – original draft, Supervision, Resources, Project administration, Funding acquisition, Conceptualization. **Peter H. Barry:** Writing – original draft, Resources, Project administration, Funding acquisition. **Suzan van der Lee:** Writing – original draft, Validation, Supervision, Resources, Project administration, Funding acquisition, Conceptualization. **John Mary Kiberu:** Resources, Project administration, Investigation, Data curation, Conceptualization. **Fred Tugume:** Resources, Project administration, Investigation, Data curation, Conceptualization. **Albert Kabanda:** Writing – original draft, Methodology, Investigation. **Michael Taylor:** Supervision, Resources, Project administration, Funding acquisition, Conceptualization. **Joan Nakajigo:** Writing – original draft, Validation. **Abbey Oluwasegun Isaac:** Investigation.

Declaration of competing interest

All authors certify that they have no affiliations with or involvement in any organization or entity with any financial interest or non-financial interest in the subject matter or materials discussed in this manuscript.

Acknowledgments

This project was supported by the National Science Foundation grant #2210214. Most of the figures in this paper were generated with Generic Mapping Tools V6.4.0 (Wessel et al., 2013). We acknowledge the gravity field crew for their hard work, including Eriya Kahwa, Nelson Birungi, Paula Babirye, Lawrence Kabenge, and Joseph Nyago. Special thanks to Georg Rümpker from the RiftLink Project for providing us with the P-velocity models. We thank the Computational Infrastructure for Geodynamics for supporting the development of ASPECT, which is funded by National Science Foundation Awards EAR-0949446 and EAR-1550901.

Appendix A. Supplementary data

Supplementary data to this article can be found online at https://doi.org/10.1016/j.tecto.2025.230881.

Data availability

The inversion codes used for this study can be obtained via subversion (https://subversion.apache.org) at svn checkout.
https://svn.code.sf.net/p/jif3d/jif3dsvn/trunk/jif3D/ jif3d. Processed data and model files can be found at https://doi.org/10.5281/zenodo.15707530.

References

Abdelsalam, M.G., Liégeois, J.P., Stern, R.J., 2002. The Saharan Metacraton. J. Afr. Earth Sci. 34, 119–136.

Abdelsalam, M.G., Gao, S.S., Liégeois, J.P., 2011. Upper mantle structure of the Saharan Metacraton. J. Afr. Earth Sci. 60 (5), 328–336.

Ajala, R., Kolawole, F., Menke, W., 2024. Blind magmatism abets nonvolcanic continental rifting. Communicat. Earth & Environ. 5 (1), 80.

Armitage, J.J., Petersen, K.D., Pérez-Gussinyé, M., 2018. The role of crustal strength in controlling magmatism and melt chemistry during rifting and breakup. Geochem. Geophys. Geosyst. 19 (2), 534–550.

Asgharzadeh, M., von Frese, R., Kim, H.R., Leftwich, T., Kim, J., 2007. Spherical prism gravity effects by Gauss-Legendre quadrature integration. Geophys. J. Int. 169 (1), 1–11. https://doi.org/10.1111/j.1365-246X.2007.03214.x.

Avdeeva, A., Avdeev, D.B., 2006. A limited-memory quasi-Newton inversion for 1D magnetotellurics. Geophysics 71, 191–196.

Bahati, G., Pang, Z., Ármannsson, H., Isabirye, E.M., Kato, V., 2005. Hydrology and reservoir characteristics of three geothermal systems in western Uganda. Geothermics 34 (5), 568–591.

Balmino, G., Vales, N., Bonvalot, S., et al., 2012. Spherical harmonic modelling to ultra-high degree of Bouguer and isostatic anomalies. J. Geod. 86, 499–520. https://doi.org/10.1007/s00190-011-0533-4.

Bangerth, W., Dannberg, J., Fraters, M., Gassmöller, R., Glerum, A., Heister, T., Myhill, R., Naliboff, J., 2023a. ASPECT v2.5.0. Zenodo [Code]. https://doi.org/10.5281/zenodo.8200213.

Bangerth, W., Dannberg, J., Fraters, M., Gassmöller, R., Glerum, A., Heister, T., Myhill, R., Naliboff, J., 2023b. ASPECT: Advanced Solver for Problems in Earth's ConvecTion. Figshare [Data set]. https://doi.org/10.6084/m9.figshare.4865333.

Batte, A.G., Rümpker, G., Lindenfeld, M., Schumann, A., 2014. Structurally controlled seismic anisotropy above small earthquakes in crustal rocks beneath the Rwenzori region, Albertine Rift, Uganda. J. Afr. Earth Sci. 100, 579–585.

Beauval, C., Yepes, H., Palacios, P., Segovia, M., Alvarado, A., Font, Y., Vaca, S., 2013. An earthquake catalog for seismic hazard assessment in Ecuador. Bull. Seismol. Soc. Am. 103 (2A), 773–786.

Begg, G.C., Griffin, W.L., Natapov, L.M., O'Reilly, S.Y., Grand, S.P., O'Neill, C.J., Bowden, P., 2009. The lithospheric architecture of Africa: Seismic tomography, mantle petrology, and tectonic evolution. Geosphere 5 (1), 23–50.

Behn, M.D., Conrad, C.P., Silver, P.G., 2004. Detection of upper mantle flow associated with the African Superplume. Earth Planet. Sci. Lett. 224 (3–4), 259–274.

Bialas, R.W., Buck, W.R., Qin, R., 2010. How much magma is required to rift a continent? Earth Planet. Sci. Lett. 292 (1–2), 68–78.

Bonvalot, S., Balmino, G., Briais, A., Kuhn, M., Peyrefitte, A., Vales, N., et al., 2012. World Gravity Map, 1:50,000,000 Map. BGI-CGMW-CNES-IRD, Paris.

Brune, S., Kolawole, F., Olive, J.A., et al., 2023. Geodynamics of continental rift initiation and evolution. Nat. Rev. Earth & Environ. 4, 235–253. https://doi.org/10.1038/s43017-023-00391-3.

Buck, W.R., 2004. Consequences of asthenospheric variability on continental rifting. In: Rheology and Deformation of the Lithosphere at Continental Margins. Columbia University Press, pp. 1–30.

Buck, W.R., 2006. The role of magma in the development of the Afro-Arabian Rift System. Geol. Soc. Lond. Spec. Publ. 259 (1), 43–54. https://doi.org/10.1144/GSL.SP.2006.259.01.05.

Calais, E., Ebinger, C., Hartnady, C., Nocquet, J.M., 2006. Kinematics of the East African Rift from GPS and earthquake slip vector data. Geol. Soc. Lond. Spec. Publ. 259, 9–22. https://doi.org/10.1144/GSL.SP.2006.259.01.03.

Clevenger, T.C., Heister, T., 2021. Comparison between algebraic and matrix-free geometric multigrid for a Stokes problem on adaptive meshes with variable viscosity. Numerical Linear Algebra with Applications 28 (e2375). https://doi.org/10.1002/nla.2375.

Colet, M., Kolawole, F., Ajala, R., Delvaux, D., Dieu-Veill Nkodia, H.M., 2025. Active crustal deformation across a nucleating extensional microplate, DR Congo, East Africa. Tectonics 44 (7), e2025TC008815.

Conrad, C.P., Behn, M.D., 2010. Constraints on lithosphere net rotation and asthenospheric viscosity from global mantle flow models and seismic anisotropy. Geochem. Geophys. Geosyst. 11 (5).

Conrad, C.P., Behn, M.D., Silver, P.G., 2007. Global mantle flow and the development of seismic anisotropy: differences between the oceanic and continental upper mantle. J. Geophys. Res. Solid Earth 112 (B7).

Corti, G., Iandelli, I., Cerca, M., 2013. Experimental modeling of rifting at craton margins. Geosphere 9, 138–154. https://doi.org/10.1130/GES00863.1.

Ebinger, C.J., 1989. Geometric and kinematic development of border faults and accommodation zones, Kivu-Rusizi Rift. Africa. Tectonics 8 (1), 117–133. https://doi.org/10.1029/TC008i001p00117.

Ebinger, C., 2005. Continental break-up: the East African perspective. Astron. Geophys. 46 (2). https://doi.org/10.1111/j.1468-4004.2005.46216.x, 2.16–2.21.

Fernandez-Alonso, M., Cutten, H., De Waele, B., Tack, L., Tahon, A., Baudet, D., Barritt, S.D., 2012. The Mesoproterozoic Karagwe-Ankole Belt (formerly the NE Kibara Belt): the result of prolonged extensional intracratonic basin development punctuated by two short-lived far-field compressional events. Precambrian Res. 216–219, 63–86. https://doi.org/10.1016/j.precamres.2012.06.007.

Feucht, D.W., Sheehan, A.F., Bedrosian, P.A., 2017. Magnetotelluric imaging of lower crustal melt and lithospheric hydration in the Rocky Mountain Front transition zone, Colorado, USA. J. Geophys. Res. Solid Earth 122 (12), 9489–9510.

Fletcher, A.W., Abdelsalam, M.G., Emishaw, L., Atekwana, E.A., Laó-Dávila, D.A., Ismail, A., 2018. Lithospheric controls on the rifting of the Tanzanian craton at the Eyasi basin, eastern branch of the East African rift system. Tectonics 37, 2818–2832. https://doi.org/10.1029/2018TC005065.

Foley, S.F., Link, K., Tiberindwa, J.V., Barifaijo, E., 2012. Patterns and origin of igneous activity around the Tanzanian craton. J. Afr. Earth Sci. 62 (1), 1–18.

Fritz, H., Abdelsalam, M.G., Ali, K.A., Bingen, B., Collins, A.S., Fowler, A.R., Ghebreab, W., Hauzenberger, C.A., Johnson, P.R., Kusky, T.M., Macey, P., Muhongo, S., Stern, R.J., Viola, G., 2013. Orogen styles in the East African Orogen: a review of the Neoproterozoic to Cambrian tectonic evolution. J. Afr. Earth Sci. 86, 65–106. https://doi.org/10.1016/j.jafrearsci.2013.06.004.

Gassmöller, R., Dannberg, J., Bangerth, W., Heister, T., Myhill, R., 2020. On formulations of compressible mantle convection. Geophys. J. Int. 221 (2), 1264–1280. https://doi.org/10.1093/gji/ggaa078.

Global Volcanism Program, 2023. Volcanoes of the World (v. 5.1.0; 9 Jun 2023), Smithsonian Institution, Compiled by Venzke, E.. https://doi.org/10.5479/si.GVP.VOTW5-2023.5.1.

Gummert, M., Lindenfeld, M., Wölbern, I., Rümpker, G., Celestin, K., Batte, A., 2016. Crustal structure and high-resolution Moho topography across the Rwenzori region (Albertine rift) from P-receiver functions. Geol. Soc. Lond. Spec. Publ. 420 (1), 69–82.

Halldórsson, S.A., Hilton, D.R., Scarsi, P., Abebe, T., Hopp, J., 2014. A common mantle plume source beneath the entire East African Rift System revealed by coupled helium-neon systematics. Geophys. Res. Lett. 41, 2304–2311. https://doi.org/10.1002/2014GL059424.

Hansen, P.C., 1992. Analysis of discrete ill-posed problems by means of the L-curve. SIAM Rev. 34 (4), 561–580. https://doi.org/10.1137/1034115.

Häuserer, M., Junge, A., 2011. Electrical mantle anisotropy and crustal conductor: a 3-D conductivity model of the Rwenzori region in western Uganda. Geophys. J. Int. 185 (3), 1235–1242. https://doi.org/10.1111/j.1365-246X.2011.05006.x.

Heister, T., Dannberg, J., Gassmöller, R., Bangerth, W., 2017. High accuracy mantle convection simulation through modern numerical methods–II: realistic models and problems. Geophys. J. Int. 210 (2), 833–851.

Homuth, B., Löbl, U., Batte, A.G., Link, K., Kasereka, C.M., Rümpker, G., 2016. Seismic anisotropy of the lithosphere/asthenosphere system beneath the Rwenzori region of the Albertine Rift. Int. J. Earth Sci. 105, 1681–1692. https://doi.org/10.1007/s00531-015-1215-5.

Jakovlev, A., Rümpker, G., Schmeling, H., Koulakov, I., Lindenfeld, M., Wallner, H., 2013. Seismic images of magmatic rifting beneath the western branch of the East African Rift. Geochem. Geophys. Geosyst. 14, 4906–4920. https://doi.org/10.1002/2013GC004939.

Kampunzu, A.B., Bonhomme, M.G., Kanika, M., 1998. Geochronology of volcanic rocks and evolution of the Cenozoic western branch of the East African Rift System. J. African Earth Sci. 26 (3), 441–461.

Karner, G.D., Byamungu, B.R., Ebinger, C.J., Kampunzu, A.B., Mukasa, R.K., Nyakaana, J., Upcott, N.M., 2000. Distribution of crustal extension and regional basin architecture of the Albertine rift system, East Africa. Mar. Pet. Geol. 17 (10), 1131–1150.

Karp, T., Scholz, C.A., McGlue, M.M., 2012. Structure and Stratigraphy of the Lake Albert Rift. Observations from seismic reflection and gravity data, East Africa.

Katumwehe, A.B., Abdelsalam, M.G., Atekwana, E.A., 2015. The role of pre-existing Precambrian structures in rift evolution: the Albertine and Rhino grabens, Uganda. Tectonophysics 646, 117–129.

Kendall, J.M., Stuart, G., Ebinger, C., et al., 2005. Magma-assisted rifting in Ethiopia. Nature 433, 146–148. https://doi.org/10.1038/nature03161.

Koehn, D., Aanyu, K., Haines, S., Sachau, T., 2008. Rift nucleation, rift propagation and the creation of basement micro-plates within active rifts. Tectonophysics 458 (1–4).

Kolawole, F., Ajala, R., 2024. Propagating rifts: the roles of crustal damage and ascending mantle fluids. Solid Earth 15 (7), 747–762.

Kolawole, F., Firkins, M., Al Wahaibi, T., Atekwana, E.A., Soreghan, M.J., 2021a. Rift transfer zones and the stages of rift linkage in active segmented continental rift systems. EarthArXiv eprints, X5J885.

Kolawole, F., Phillips, T.B., Atekwana, E.A., Jackson, C.A., 2021b. Structural inheritance controls strain distribution during early continental rifting, Rukwa Rift. Frontiers in Earth Science 9, 707869.

Koptev, A., Calais, E., Burov, E., et al., 2015. Dual continental rift systems generated by plume–lithosphere interaction. Nat. Geosci. 8, 388–392. https://doi.org/10.1038/ngeo2401.

Kronbichler, M., Heister, T., Bangerth, W., 2012. High accuracy mantle convection simulation through modern numerical methods. Geophys. J. Int. 191 (1), 12–29.

Lærdal, T, and M.R. Talbot (2002). Basin neotectonics of Lakes Edward and George, East African Rift. Paleogeography, Paleoclimatology, Paleoecology 187, 213–232, doi: https://doi.org/10.1016/S0031-0182(02)00478-9.

Leseane, K., Atekwana, E.A., Mickus, K.L., Abdelsalam, M.G., Shemang, E.M., Atekwana, E.A., 2015. Thermal perturbations beneath the incipient Okavango Rift Zone, Northwest Botswana. J. Geophys. Res. Solid Earth 120, 1210–1228. https://doi.org/10.1002/2014JB011029.

Lindenfeld, M., Rümpker, G., Link, K., Koehn, D., Batte, A., 2012. Fluid-triggered earthquake swarms in the Rwenzori region, East African Rift—evidence for rift initiation. Tectonophysics 566, 95–104.

Link, K., Koehn, D., Barth, M.G., Tiberindwa, J.V., Barifaijo, E., Aanyu, K., Foley, S.F., 2010. Continuous cratonic crust between the Congo and Tanzania blocks in western Uganda. Int. J. Earth Sci. 99, 1559–1573. https://doi.org/10.1007/s00531-010-0548-8.

Lösing, M., Moorkamp, M., Ebbing, J., 2023. Joint inversion based on variation of information—a crustal model of Wilkes Land. East Antarctica. Geophys. J. Int. 232 (1), 162–175.

Lowe, M., Jordan, T., Moorkamp, M., Ebbing, J., Green, C., Lösing, M., Larter, R., 2024. The 3D crustal structure of the Wilkes Subglacial Basin, East Antarctica, using variation of information joint inversion of gravity and magnetic data. Journal of Geophysical Research: Solid. Earth 129 (10), e2023JB027794.

Mickus, K., Tadesse, K., Keller, G.R., Oluma, B., 2007. Gravity analysis of the main Ethiopian rift. J. Afr. Earth Sci. 48 (2–3), 59–69.

Moorkamp, M., Jegen, M., Roberts, A., Hobbs, R., 2010. Massively parallel forward modeling of scalar and tensor gravimetry data. Comput. Geosci. 36 (5), 680–686.

Moorkamp, M., Heincke, B., Jegen, M., Roberts, A.W., Hobbs, R.W., 2011. A framework for 3-D joint inversion of MT, gravity and seismic refraction data. Geophys. J. Int. 184, 477–493. https://doi.org/10.1111/j.1365-246X.2010.04856.x.

Muirhead, J.D., Wright, L.J., Scholz, C.A., 2019. Rift evolution in regions of low magma input in East Africa. Earth Planet. Sci. Lett. 506, 332–346.

Murphy, B.S., DeLucia, M.S., Marshak, S., Ravat, D., Bedrosian, P.A., 2024. Magnetotelluric insights into the formation and reactivation of trans-crustal shear zones in Precambrian basement of the eastern US Midcontinent. Geol. Soc. Am. Bull. 136 (7–8), 2661–2675.

Njinju, E.A., 2016. Crustal and Sub-Continental Lithospheric Mantle Decoupling beneath the Malawi Rift (Master's thesis,. Oklahoma State University.

Njinju, E.A., Atekwana, E.A., 2025. A gravity study of the crustal structure beneath the young amagmatic Rukwa-Tanganyika rift zone. Tectonics 44 (8), e2024TC008722.

Njinju, E.A., Atekwana, E.A., Stamps, D.S., Abdelsalam, M.G., Atekwana, E.A., Mickus, K. L., et al., 2019a. Lithospheric structure of the Malawi Rift: Implications for magma-poor rifting processes. Tectonics 38, 3835–3853. https://doi.org/10.1029/2019TC005549.

Njinju, E.A., Kolawole, F., Atekwana, E.A., Stamps, D.S., Atekwana, E.A., Abdelsalam, M. G., Mickus, K.L., 2019b. Terrestrial heat flow in the Malawi Rifted Zone, East Africa: Implications for tectono-thermal inheritance in continental rift basins. J. Volcanol. Geotherm. Res. 387, 106656.

Njinju, E.A., Stamps, D.S., Neumiller, K., Gallager, J., 2021. Lithospheric control of melt generation beneath the Rungwe Volcanic Province, East Africa: Implications for a plume source. J. Geophys. Res. Solid Earth 126, e2020JB020728. https://doi.org/10.1029/2020JB020728.

Njinju, E.A., Stamps, D.S., Atekwana, E.A., Rooney, T.O., Rajaonarison, T.A., 2023a. Instantaneous 3D tomography-based convection beneath the Rungwe Volcanic Province, East Africa: implications for melt generation. Geophys. J. Int. 235 (1), 296–311.

Njinju, E.A., Moorkamp, M., Stamps, D.S., 2023b. Density structure beneath the Rungwe volcanic province and surroundings, East Africa from shear-wave velocity perturbations constrained inversion of gravity data. Front. Earth Sci. 11, 1118566.

Njinju, E.A., Kolawole, F., Stamps, D.S., Atekwana, E.A., Ghomsi, F.E.K., Atekwana, E.A., 2025. Intrarift fault interactions: Insights from coseismic stress redistribution from large seismogenic segment ruptures, Northern Malawi Rift. J. Struct. Geol. 191, 105326.

Nyakecho, C., Hagemann, S.G., 2014. An overview of gold systems in Uganda. Aust. J. Earth Sci. 61, 59–88. https://doi.org/10.1080/08120099.2013.831773.

Nyalugwe, V.N., Abdelsalam, M.G., Atekwana, E.A., Katumwehe, A., Mickus, K.L., Salima, J., Njinju, E.A., Emishaw, L., 2019. Lithospheric structure beneath the cretaceous Chilwa alkaline province (CAP) in southern Malawi and northeastern Mozambique. J. Geophys. Res. Solid Earth 124 (11), 12224–12240.

Paulatto, M., Moorkamp, M., Hautmann, S., Hooft, E., Morgan, J.V., Sparks, R.S.J., 2019. Vertically extensive magma reservoir revealed from joint inversion and quantitative interpretation of seismic and gravity data. J. Geophys. Res. Solid Earth 124 (11), 11170–11191.

Phipps Morgan, J., Holtzman, B.K., 2005. Vug waves: a mechanism for coupled rock deformation and fluid migration. Geochem. Geophys. Geosyst. 6 (8).

Pickford, M., Senut, B., Hadoto, D., 1993. Geology and palaeobiology of the Albertine Rift Valley, Uganda-Zaire. Volume I: Geology. Publication Occasionnelle-Centre International pour la Formation et les Échanges Géologiques, 24.

Rajaonarison, T.A., Stamps, D.S., Naliboff, J., Nyblade, A., Njinju, E.A., 2023. A geodynamic investigation of plume-lithosphere interactions beneath the East African rift. J. Geophys. Res. Solid Earth 128 (4), e2022JB025800.

Ring, U., 2008. Extreme uplift of the Rwenzori Mountains in the East African Rift, Uganda: Structural framework and possible role of glaciations. Tectonics 27, TC4018. https://doi.org/10.1029/2007TC002176.

Ritsema, J., Deuss, A., van Heijst, H.J., Woodhouse, J.H., 2011. S40RTS: a degree-40 shear-velocity model for the mantle from new Rayleigh wave dispersion, teleseismic traveltime, and normal-mode splitting function measurements. Geophys. J. Int. 184 (3), 1223–1236. https://doi.org/10.1111/j.1365-246X.2010.04884.x.

Roberts, E.M., Stevens, N.J., O'Conner, P.M., Dirks, P.H.G.M., Gottfried, M.D., Clyde, W. C., Armstrong, R.A., Kemp, A.I.S., Hemming, S., 2012. Initiation of the western branch of the East African Rift coeval with the eastern branch. Nat. Geosci. 5, 289–294.

Roller, S., Hornung, J., Hinderer, M., Ssemmanda, I., 2010. Middle Miocene to Pleistocene sedimentary record of rift evolution in the southern Albert Rift (Uganda). Int. J. Earth Sci. 99, 1643–1661.

Rooney, T.O., Herzberg, C., Bastow, I.D., 2012. Elevated mantle temperature beneath East Africa. Geology 40, 27–30. https://doi.org/10.1130/G32382.1.

Rosenthal, A., Foley, S.F., Pearson, D.G., Nowell, G.M., Tappe, S., 2009. Petrogenesis of strongly alkaline primitive volcanic rocks at the propagating tip of the Western Branch of the East African Rift. Earth Planet. Sci. Lett. 284, 236–248. https://doi.org/10.1016/j.epsl.2009.04.036.

Sachau, T., Koehn, D., Stamps, D.S., Lindenfeld, M., 2016. Fault kinematics and stress fields in the Rwenzori Mountains, Uganda. Int. J. Earth Sci. 105, 1729–1740.

Saria, E., Calais, E., Stamps, D., Delvaux, D., Hartnady, C., 2014. Present-day kinematics of the East African Rift. J. Geophys. Res. Solid Earth 119, 3584–3600. https://doi.org/10.1002/2013JB010901.

Schmeling, H., 2010. Dynamic models of continental rifting with melt generation. Tectonophysics 480 (1–4), 33–47.

Simiyu, S.M., Keller, G.R., 2001. An integrated geophysical analysis of the upper crust of the southern Kenya Rift. Geophys. J. Int. 147 (3), 543–561. https://doi.org/10.1046/j.0956-540x.2001.01542.x.

Simon, B., Guillocheau, F., Robin, C., Dauteuil, O., Nalpas, T., Pickford, M., Senut, B., Lays, P., Bourges, P., Bez, M., 2017. Deformation and sedimentary evolution of the Lake Albert Rift (Uganda, East African Rift System). Mar. Pet. Geol. 86, 17–37. https://doi.org/10.1016/j.marpetgeo.2017.05.006.

Stamps, D.S., Calais, E., Saria, E., Hartnady, C., Nocquet, J.M., Ebinger, C., Fernandes, R. M., 2008. A kinematic model for the East African Rift. Geophys. Res. Lett. 35, L05304. https://doi.org/10.1029/2007GL032781.

Stamps, D.S., Flesch, L.M., Calais, E., 2010. Lithospheric buoyancy stresses in Africa from a thin sheet approach. Int. J. Earth Sci. 99 (7), 1309–1317. https://doi.org/10.1007/s00531-010-0533-2.

Stamps, D.S., Flesch, L.M., Calais, E., Ghosh, A., 2014. Current kinematics and dynamics of Africa and the East African Rift. J. Geophys. Res. 119, 4929–4946. https://doi.org/10.1002/2013JB010717.

Stamps, D.S., Saria, E., Kreemer, C., 2018. A geodetic strain rate model for the East African Rift System. Sci. Rep. 8 (1), 732.

Stamps, D.S., Kreemer, C., Fernandes, R., Rajaonarison, T.A., Rambolamanana, G., 2021. Redefining East African Rift system kinematics. Geology 49 (2), 150–155.

Stuart, C.A., Piazolo, S., Daczko, N.R., 2016. Mass transfer in the lower crust: evidence for incipient melt-assisted flow along grain boundaries in the deep arc granulites of Fiordland, New Zealand. Geochem. Geophys. Geosyst. 17 (9), 3733–3753.

Styron, R., Pagani, M., 2020. The GEM global active faults database. Earthquake Spectra 36 (1_suppl), 160–180.

Tack, L., Wingate, M.T.D., De Waele, B., Meert, J., Belousova, E., Griffin, B., Tahon, A., Fernandez-Alonso, M., 2010. The 1375Ma "Kibaran event" in Central Africa: Prominent emplacement of bimodal magmatism under extensional regime. Precambrian Res. 180, 63–84. https://doi.org/10.1016/j.precamres.2010.02.022.

Telford, W.M., Geldart, L.P., Sheriff, R.E., 1990. Applied Geophysics. Cambridge University Press.

Uieda, L., Barbosa, V.C.F., 2016. A gravity-derived Moho model for South America: source code, data, and model results from "Fast non-linear gravity inversion in spherical coordinates with application to the South American Moho.". Figshare [Dataset]. https://doi.org/10.6084/m9.figshare.3987267.v1.

Uieda, L., Barbosa, V.C.F., 2017. Fast nonlinear gravity inversion in spherical coordinates with application to the South American Moho. Geophys. J. Int. 208 (1), 162–176.

Upcott, N.M., Mukasa, R.K., Ebinger, C.J., Karner, G.D., 1996. Along-axis segmentation and isostasy in the Western Rift. East Africa. J. Geophys. Res. 101 (B1), 3247–3268. https://doi.org/10.1029/95JB01480.

Wallner, H., Schmeling, H., 2010. Rift induced delamination of mantle lithosphere and crustal uplift: a new mechanism for explaining Rwenzori Mountains' extreme elevation? Int. J. Earth Sci. 99, 1511–1524.

Wedmore, L.N., et al., 2024. The early onset of magmatic rift faulting in the Edward-George Rift. Uganda. Earth Planet. Sci. Let. 638, 118762. https://doi.org/10.1016/j.epsl.2024.118762.

Wessel, P., Smith, W.H.F., Scharroo, R., Luis, J., Wobbe, F., 2013. Generic Mapping Tools: improved Version Released. Eos Trans. AGU 94 (45), 409.

Westerhof, P.A.B., Paavo, H., Isabirye, E., Katto, E., Koistinen, T., Kuosmanen, E., Lehto, T., Matti, I., Lehtonen, H., Mäkitie, T., Manninen, I., Mänttäri, Y., Pekkala, J., Pokki, K. Saalmann, Virransalo, P., 2014. Geology and Geodynamic Development of Uganda with Explanation of the 1:1,000,000 -Scale Geological Map. Geol. Survey of Finland, Technical report number 55, 2014.

Wilson, J.T., 1966. Did the Atlantic Close and then Re-Open? Nature 211, 676–681.

Wölbern, I., Rümpker, G., Schumann, A., Muwanga, A., 2010. Crustal thinning beneath the Rwenzori region, Albertine Rift, Uganda, from receiver-function analysis. Int. J. Earth Sci. 99, 1545–1557.

Wölbern, I., Rümpker, G., Link, K., Sodoudi, F., 2012. Melt infiltration of the lower lithosphere beneath the Tanzania craton and the Albertine Rift inferred from S receiver functions. Geochem. Geophys. Geosyst. 13 (8).

Xue, L., Gani, N.D., Abdelsalam, M.G., 2017. Geomorphologic proxies for bedrock rivers: a case study from the Rwenzori Mountains, East African Rift System. Geomorphology 285, 374–398.

Yu, Y., Liu, K.H., Reed, C.A., Moidaki, M., Mickus, K., Atekwana, E.A., Gao, S.S., 2015. A joint receiver function and gravity study of crustal structure beneath the incipient Okavango Rift, Botswana. Geophys. Res. Lett. 42, 8398–8405. https://doi.org/10.1002/2015GL065811.

Zhdanov, M.S., 2002. Geophysical Inverse Theory and Regularization Problems, vol. 36. Elsevier.